









The μ Tau Association: A 60 Myr Old Coeval Group at 150 pc from the Sun

Jonathan Gagné^{1,2} , Trevor J. David^{3,4} , Eric E. Mamajek^{4,5} , Andrew W. Mann⁶ , Jacqueline K. Faherty⁷ , and Antoine Bédard⁸ 

¹ Planétarium Rio Tinto Alcan, Espace pour la Vie, 4801 av. Pierre-de Coubertin, Montréal, QC, Canada; gagne@astro.umontreal.ca

² Institute for Research on Exoplanets, Université de Montréal, Département de Physique, C.P. 6128 Succ. Centre-ville, Montréal, QC H3C 3J7, Canada

³ Center for Computational Astrophysics, Flatiron Institute, New York, NY 10010, USA

⁴ Jet Propulsion Laboratory, California Institute of Technology, 4800 Oak Grove Drive, Pasadena, CA 91109, USA

⁵ Department of Physics & Astronomy, University of Rochester, Rochester, NY 14627, USA

⁶ Department of Physics and Astronomy, University of North Carolina at Chapel Hill, Chapel Hill, NC 27599-3255, USA

⁷ Department of Astrophysics, American Museum of Natural History, Central Park West at 79th St., New York, NY 10024, USA

⁸ Département de Physique, Université de Montréal, C.P. 6128 Succ. Centre-ville, Montréal, QC H3C 3J7, Canada

Received 2020 June 5; revised 2020 August 13; accepted 2020 August 13; published 2020 November 6

Abstract

We present an analysis of the newly identified μ Tau Association (MUTA) of young stars at $\simeq 150$ pc from the Sun that is part of the large Cas-Tau structure, coeval and comoving with the α Persei cluster. This association is also located in the vicinity of the Taurus-Auriga star-forming region and the Pleiades association, although it is unrelated to them. We identify more than 500 candidate members of MUTA using Gaia DR2 data and the BANYAN Σ tool, and we determine an age of 62 ± 7 Myr for its population based on an empirical comparison of its color–magnitude diagram sequence with those of other nearby young associations. The MUTA association is related to the Theia 160 group of Kounkel & Covey and corresponds to the e Tau group of Liu et al. It is also part of the Cas-Tau group of Blaauw. As part of this analysis, we introduce an iterative method based on spectral templates to perform an accurate correction of interstellar extinction of Gaia DR2 photometry, needed because of its wide photometric bandpasses. We show that the members of MUTA display an expected increased rate of stellar activity and faster rotation rates compared with older stars, and that literature measurements of the lithium equivalent width of nine G0- to K3-type members are consistent with our age determination. We show that the present-day mass function of MUTA is consistent with other known nearby young associations. We identify WD 0340+103 as a hot, massive white dwarf remnant of a B2 member that left its planetary nebula phase only 270,000 yr ago, posing an independent age constraint of 60^{+8}_{-6} Myr for MUTA, consistent with our isochrone age. This relatively large collection of comoving young stars near the Sun indicates that more work is required to unveil the full kinematic structure of the complex of young stars surrounding α Persei and Cas-Tau.

Unified Astronomy Thesaurus concepts: [Astrometry \(80\)](#); [Stellar associations \(1582\)](#); [Proper motions \(1295\)](#); [Brown dwarfs \(185\)](#); [Stellar kinematics \(1608\)](#); [Low mass stars \(2050\)](#)

Supporting material: data behind figure, figure set, machine-readable tables

1. Introduction

Young stellar associations in the solar neighborhood ($\lesssim 200$ pc) are valuable laboratories to study stellar evolution and refine our age-dating methods because they contain groups of stars with many different masses that formed coevally from the same molecular cloud (e.g., Zuckerman & Song 2004; Torres et al. 2008). Their proximity is valuable because their members appear brighter, but it also causes them to be spread over larger areas of the sky, which makes their initial identification less straightforward. Obtaining credible lists of members with low contamination by unrelated field stars is challenging and typically requires measuring the six-dimensional position and space velocity of each member. As these stars formed from a single molecular cloud, they share the same velocities typically within $\simeq 2\text{--}4$ km s^{−1}, allowing us to distinguish them from most field stars.

Until recently, trigonometric distance measurements were only available for a limited set of bright stars (e.g., Perryman et al. 1997), and radial velocity measurements of stars in the solar neighborhood were even more limited to small-scale samples (see, e.g., Gontcharov 2006; White et al. 2007). This led to the identification of comoving and coeval massive stars that represented only the tip of the iceberg of each young

association of stars in our neighborhood (Zuckerman & Song 2004; Torres et al. 2008). Efforts have been made to identify the lower-mass population based on various methods that can assign membership probabilities with missing parts of the six-dimensional space and velocity, including the convergent point method (Mamajek 2005; Torres et al. 2006) and various other flavors of selection cuts in space velocity and/or photometry (Zuckerman & Song 2004; Kraus et al. 2014; Riedel et al. 2017; Shkolnik et al. 2017), as well as methods based on Bayesian statistics (Malo et al. 2013; Gagné et al. 2014, 2018c).

The second data release of the Gaia mission (hereafter Gaia DR2; Gaia Collaboration et al. 2018; Lindegren et al. 2018)⁹ changed this landscape completely in 2018 April by providing trigonometric distance measurements for $\simeq 1.3$ billion stars with an unprecedented precision, as well as radial velocities for more than 7.2 million bright stars. This allowed us to complete the six-dimensional kinematics for a number of stars on a completely new scale, which led to a plethora of scientific

⁹ See also Luri et al. (2018), Mignard et al. (2018), Babusiaux et al. (2018), Sartoretti et al. (2018), Soubiran et al. (2018), Cropper et al. (2018), Evans et al. (2018b), Hambly et al. (2018), and Riello et al. (2018) for relevant calibration.

discoveries that quickly unveiled the spatial and kinematic structure of the solar neighborhood, as well as the Milky Way in general. Some of these discoveries include many new associations of stars (Oh et al. 2017; Faherty et al. 2018; Gagné et al. 2018a; Kounkel & Covey 2019; Meingast et al. 2019), a large number of new M-type members of known associations (Gagné & Faherty 2018; Gagné et al. 2018d; Luhman 2018; Reino et al. 2018; Tang et al. 2019; Zuckerman 2019), and the discovery of tidal disruption tails around three older, nearby clusters: the Hyades (Röser et al. 2019), Praesepe (Röser & Schilbach 2019), and Coma Ber (Tang et al. 2019).

This paper presents the discovery and characterization the MUTA association, based on an initial list of massive comoving and coeval members that had been discovered in historical surveys but have never before been published. The advent of Gaia DR2 allowed us to complete this list and characterize MUTA such that it will become yet another important laboratory for the investigation of stellar evolution and the grounds for discovery of age-calibrated brown dwarfs and exoplanets. In Section 2, we present the initial list of MUTA members, which we use to build a spatial-kinematic model (Section 3) to search for additional members with the BANYAN Σ Bayesian identification tool (Gagné et al. 2018c) in Section 4. In Section 5, we present an iterative method to correct interstellar extinction in Gaia DR2 color–magnitude diagrams, required because the photometric bandpasses are wider than usual. We discuss the properties of MUTA as a whole and its individual members in Section 6, including their present-day mass function and stellar activity indicators, as well as a comparison with the Galactic kinematic structures recently unveiled by Kounkel & Covey (2019). We summarize and conclude this work in Section 7.

2. Initial Sample of Members

The existence of a distinct group of comoving young stars in the vicinity of the Taurus-Auriga (Kenyon et al. 2008) star-forming region first appeared in a spatial distribution of Cas-Tau OB-type stars assembled by Blaauw (1956). Cas-Tau was identified by Blaauw (1956) as an extended group of comoving stars with an expansion age of $\simeq 50$ Myr that seems to be on the way to being dissolved. They noted that Cas-Tau may share a common origin with an extended stream of stars around the α Persei cluster (see, e.g., Heckmann & Lübeck 1958; Lodieu et al. 2019) identified by Rasmuson (1921). An overdensity in the Cas-Tau stars seemed to be located at Galactic coordinates $(\ell, b) = (190^\circ, -10^\circ)$ and was recovered as part of the de Zeeuw et al. (1999) census of nearby OB associations (see their Figure 19). This overdensity overlaps with subgroup 5 of Cas-Tau defined by Blaauw (1956), with five B-type stars in common (29 Tau, 30 Tau, 35 Eri, μ Tau, μ Eri) and one additional star (40 Tau) not in common that seems to be an unrelated background star. Combining this list of 12 early-type stars assembled by de Zeeuw et al. (1999) with other comoving B-, A-, and F-type stars in the range of ℓ from 170° to 205° and b from -40° to -27° , as well as nearby ROSAT entries (Boller et al. 2016) in the same region, yielded a total set of 35 stars that appeared to be young and comoving within 15 mas yr^{-1} of the average proper motions of the de Zeeuw et al. (1999) list ($\mu_\alpha \cos \delta = 21.0 \text{ mas yr}^{-1}$, $\mu_\delta = -20.5 \text{ mas yr}^{-1}$). Four of these 37 stars are clear outliers in either XYZ (HD 23110, TYC 657–794–2, and HD 28796) or UVW (HIP 18778) and

were excluded from our initial list. The resulting 33 stars are listed in Table 1 with their properties. We tentatively named this group the μ Tau Association (MUTA) after one of its brightest members. We assigned initial members with MUTA identification numbers (from 1 to 30) in order of decreasing V-band brightness. We assigned the same MUTA ID to binaries with separations below $15''$.

In a more recent analysis of the Gaia Data Release 1 (DR1), Oh et al. (2017) recovered about a third of the stars in Table 1 as three broken-up groups of comoving systems, which they named Groups 43 (six matches), 52 (three matches), and 60 (four matches). The overlap between our initial list of MUTA members and the Oh et al. (2017) sample is shown in Figure 1, where part of the Taurus star-forming region can be seen at a similar distance from the Sun (see, e.g., Wichmann et al. 2000), and the Hyades cluster (Perryman et al. 1998) also appears in the foreground. The method that Oh et al. (2017) used to identify systems of comoving stars works directly in proper motion and parallax space, which tends to recover spatially large moving groups only as broken parts, explaining why the spatially extended MUTA was broken up in three groups, similarly to other nearby young moving groups (Faherty et al. 2018).

We cross-matched our initial list of MUTA members with Gaia DR2 data to build a color–magnitude sequence shown in Figure 2 to demonstrate that they constitute massive OBA-type stars ($G - G_{\text{RP}} < 0.2$) and a well-defined sequence of later-type stars ($G - G_{\text{RP}} > 0.2$), providing further evidence that they are coeval and young.

The earliest-type member in our initial list is 29 Tau (MUTA 5), a B3 V-type star (Beavers & Cook 1980), which corresponds to a mass of $\simeq 5.4 M_\odot$ (Pecaut & Mamajek 2013). Hohle et al. (2010) and Gullikson et al. (2016) estimated the mass of 29 Tau based on evolutionary tracks and found respective values of $6.0 \pm 0.7 M_\odot$ and $5.4 \pm 0.6 M_\odot$, consistent with the expected mass for a B3 star. Following the evolutionary tracks of Choi et al. (2016), such a star has a main-sequence life of only $\simeq 80$ Myr, indicating that MUTA is likely younger than the Pleiades.

We note that both μ Tau (MUTA 2) and τ^1 Ari are known eclipsing binaries (Avvakumova et al. 2013). While the first is part of our initial list of members, τ^1 Ari was identified in an earlier parsing of de Zeeuw et al. (1999) but was not included because of its discrepant UVW motion (it is separated from the other stars by $\simeq 6.3 \text{ km s}^{-1}$). A further analysis of their respective light curves might be useful for constraining models of stellar structure at young ages.

3. A Kinematic Model of MUTA Members

The BANYAN Σ tool (Gagné et al. 2018c) makes it possible to identify additional stars with similar Galactic positions XYZ and space velocities UVW compared to our initial list of MUTA members, if we provide it with a six-dimensional multivariate Gaussian model for MUTA in XYZUVW space. One of the main benefits of BANYAN Σ is its ability to recover stars with only partial kinematics, often a consequence of missing radial velocity or parallax measurements. The BANYAN Σ tool currently includes kinematic models for 29 nearby young associations, which consist of the 27 associations described in Gagné et al. (2018c), as well as the recently discovered Volans-Carina association (Gagné et al. 2018a) and the Argus

Table 1
Initial Members of MUTA

MUTA ID	Name	Spectral Type	R.A. (hh:mm:ss.sss)	Decl. (dd:mm:ss.ss)	Distance ^a (pc)	Gaia DR2 G mag	References ^b
1	μ Eri	B3+A3	04:45:30.167	-03:15:16.97	160 \pm 5	3.931 \pm 0.004	16
2	μ Tau	B3IV	04:15:32.079	+08:53:32.14	149 \pm 7	4.183 \pm 0.003	5
3 A	30 Tau	B3V	03:48:16.292	+11:08:35.52	129 \pm 3	5.040 \pm 0.002	5
3 B	TYC 661-1404-1	F5+F5	03:48:16.835	+11:08:40.16	138 \pm 1	9.2693 \pm 0.0002	2
4	35 Eri	B5V	04:01:32.077	-01:32:59.02	133 \pm 3	5.230 \pm 0.002	5
5	29 Tau	B3+A7	03:45:40.466	+06:02:59.78	187 \pm 9	5.295 \pm 0.001	4
6	HD 28375	B5V	04:28:32.142	+01:22:50.65	146 \pm 4	5.491 \pm 0.001	14
7	HD 28843	B9III	04:32:37.573	-03:12:34.60	169 \pm 3	5.740 \pm 0.002	15
8	HD 19698	B8V	03:10:38.828	+11:52:21.07	134 \pm 2	5.9439 \pm 0.0008	1
9	HR 1307	B8V	04:13:34.588	+10:12:44.52	144 \pm 3	6.1900 \pm 0.0006	13
10	V766 Tau	B9	03:51:15.896	+13:02:45.52	161 \pm 2	6.247 \pm 0.001	9
11	HD 28715	B9	04:31:50.463	+05:45:51.74	187 \pm 4	6.6396 \pm 0.0004	3
12	HD 24456	B9.5V	03:53:30.257	+02:07:08.57	138.7 \pm 0.9	6.6983 \pm 0.0004	10
13	HD 23990	B9.5V	03:49:46.521	+09:24:26.60	147 \pm 1	6.7410 \pm 0.0004	6
14	HD 23538	A0	03:46:26.278	+13:30:32.46	168 \pm 2	6.8479 \pm 0.0003	3
15	HD 25978	B9V	04:07:11.204	+12:16:05.10	166 \pm 2	7.6661 \pm 0.0003	12
16	HD 26323	A2V	04:10:06.873	+07:41:52.12	161 \pm 2	8.5401 \pm 0.0005	10
17	HD 27687	A3	04:22:24.213	+06:31:45.14	165 \pm 1	8.9125 \pm 0.0004	3
18	HD 28356	A3	04:28:32.733	+06:05:52.07	157 \pm 2	8.9675 \pm 0.0004	3
19 A	HD 23376	G5	03:44:58.957	+08:19:10.09	145 \pm 1	9.2549 \pm 0.0003	3
19 B	TYC 658-1007-2	...	03:44:59.048	+08:19:13.81	142 \pm 1	10.493 \pm 0.002	...
20	HIP 17133	A0	03:40:09.988	+13:11:55.07	150 \pm 1	9.949 \pm 0.001	3
21	HD 286374	F5	03:56:19.224	+11:25:10.84	152 \pm 2	9.9776 \pm 0.0005	11
22	PPM 119410	F8	03:50:50.558	+11:00:05.12	151 \pm 1	10.0929 \pm 0.0006	8
23	TYC 1248-394-1	G5IV	03:50:28.436	+16:31:14.80	146 \pm 1	10.364 \pm 0.001	7
24	RX J0348.5+0832	G7	03:48:31.461	+08:31:36.43	152 \pm 2	10.841 \pm 0.002	2
25	TYC 80-202-1	...	04:15:51.119	+07:07:03.76	167 \pm 1	10.8894 \pm 0.0006	...
26	TYC 662-217-1	...	03:59:42.158	+12:10:08.14	148 \pm 1	11.111 \pm 0.002	...
27	RX J0338.3+1020	G9	03:38:18.266	+10:20:16.32	146 \pm 1	10.976 \pm 0.001	2
28	TYC 664-136-1	...	03:51:39.673	+14:47:47.84	160 \pm 1	11.566 \pm 0.002	...
29	RX J0358.2+0932	K3	03:58:12.749	+09:32:21.97	146.8 \pm 0.9	12.045 \pm 0.001	2
30 A	TYC 668-737-1	...	04:21:24.386	+08:53:54.34	151 \pm 1	11.356 \pm 0.002	...
30 B	2MASS J04212444+0853488	...	04:21:24.473	+08:53:48.52	151 \pm 1	14.7603 \pm 0.0007	...

Notes. See Section 2 for more details.

^a Gaia DR2 distances assuming a 0.029 mas zero-point (Lindgren et al. 2018).

^b References for spectral types.

References. (1) Cowley et al. 1969; (2) Magazzù et al. 1997; (3) Cannon & Pickering 1993; (4) Beavers & Cook 1980; (5) Lesh 1968; (6) Abt 2008; (7) White et al. 2007; (8) Wright et al. 2003; (9) Cowley 1968; (10) Grenier et al. 1999; (11) Nesterov et al. 1995; (12) Bidelman et al. 1988; (13) Cowley 1972; (14) Molnar 1972; (15) Jaschek & Jaschek 1980; (16) van Leeuwen 2007.

(This table is available in machine-readable form.)

association (Makarov & Urban 2000), whose census of members was recently revised by Zuckerman (2019).

We compiled literature radial velocity measurements for the stars listed in Table 1 to identify a set of 25 core members with complete kinematics (see Table 2). This list excludes any gravitationally bound companion to avoid artificially giving each system more weight in the kinematic construction of the MUTA model (consistent with the model construction method of Gagné et al. 2018c). HD 28715, HD 23990, HD 23538, and HD 27687 (MUTA 11, 13, 14, and 17, respectively) currently do not have radial velocity measurements and were not included in Table 2, although they are likely part of MUTA based on their position in the color–magnitude diagram (see Figure 2) and their common proper motion and parallax compared to the other members.

The methodology described in Gagné et al. (2018; see their Section 5) was used to build an $XYZUVW$ multivariate

Gaussian model of the stars listed in Table 2. In summary, a six-dimensional average vector and covariance matrix in $XYZUVW$ space was built by calculating the average, variance, and covariances of the 25 core members with full kinematics listed in Table 2. When calculating the averages, variances, and covariances, the individual measurements were weighted proportionally to the squared inverse of their individual error bars to minimize the impact of low-quality measurements. The covariance matrix is then regularized to ensure that its determinant is finite and positive with a singular value decomposition step. The resulting model is shown in Figure 3.

The multivariate Gaussian model in $XYZUVW$ space that was found to best represent MUTA has the following central position \bar{x}_0 and covariance matrix $\bar{\Sigma}$:

$$\bar{x}_0 = [-130.7 \ 0.2 \ -79.7 \ -14.15 \ -24.20 \ -6.21],$$

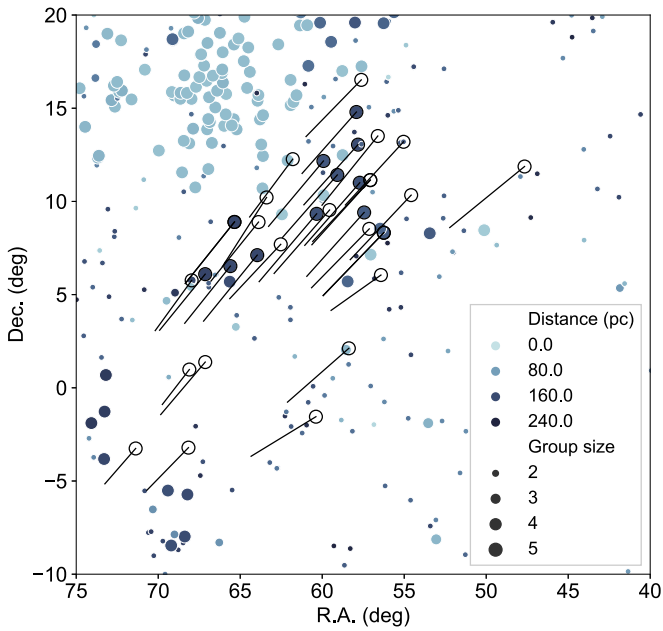


Figure 1. Sky position and proper motions of MUTA members (open circles with proper-motion arrows), compared with nearby comoving systems recovered by Oh et al. (2017; filled blue circles). The larger circles belong to Oh et al. (2017) comoving systems with more members (the maximum symbol size indicates five or more members), and the darker-shaded circles correspond to objects farther away from the Sun. The tip of the Taurus star-forming region can be seen as large, dark-blue circles at R.A. $\approx 55^\circ$ – 60° , decl. $\approx 20^\circ$, and part of the foreground Hyades cluster can be seen as large, light-blue circles at R.A. $\approx 65^\circ$ – 75° , decl. $\approx 10^\circ$ – 20° . See Section 2 for more details.

$$\bar{\Sigma} = \begin{bmatrix} 478 & 286 & 196 & 16 & 11.9 & 15 \\ 286 & 432 & 136 & 6.7 & 7.6 & 6.0 \\ 196 & 136 & 155 & 5.2 & 4.7 & -3.9 \\ 16 & 6.7 & 5.2 & 9.1 & 0.46 & 5.5 \\ 12 & 7.6 & 4.7 & 0.46 & 2.8 & 0.76 \\ 15 & 6.0 & -3.9 & 5.5 & 0.76 & 5.9 \end{bmatrix},$$

both in units of parsecs and kilometers per second.

The average sky position of MUTA members is 04:01:29.54, +07:59:33.3 (60°3731, 7°9926) with a standard deviation of 5° in both directions. The average galactic coordinates (ℓ , b) are (182°4658, -31° 8645) with a standard deviation of (9°, 3°). The average total velocity S_{tot} of the members is 28.3 km s $^{-1}$ with a standard deviation of 2.3 km s $^{-1}$. The UVW values we find correspond to a convergent point of 103°380, -29° 325 in R.A. and decl. (06:53:31, -29° 19:30).

4. A Search for Additional Members

The kinematic model described in Section 3 was combined with the BANYAN Σ tool to identify candidate members of MUTA in Gaia DR2 data. We preselected only Gaia DR2 entries with right ascensions in the range 10°–150°, declinations in the range -20° to $+40^\circ$, and trigonometric distances within 300 pc of the Sun. These limits are significantly wider than the ranges of sky positions (47° – 72° and -3° 5 to 16°5, respectively) and distances (all in the range 130–220 pc) of the initial list of members. The sky positions, proper motions, and parallaxes from Gaia DR2 were used to determine a membership probability, as well as the Gaia DR2 radial velocities when available. We selected only the stars with Bayesian membership probabilities above 90% and a maximum likelihood separation of less than 5 km s $^{-1}$ from the core of our MUTA

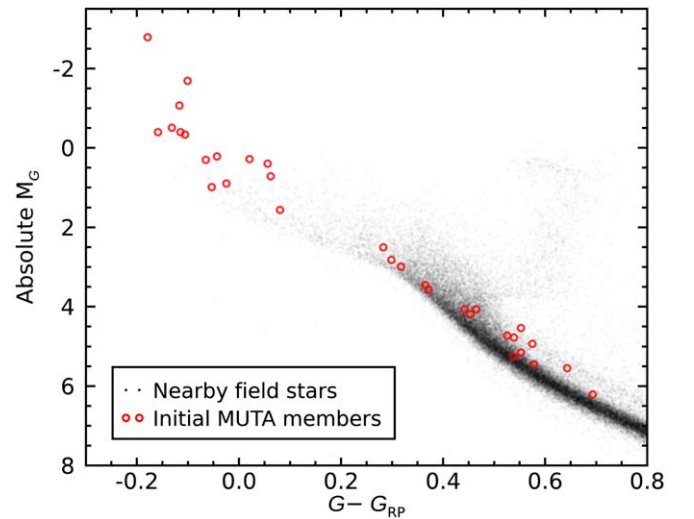


Figure 2. Gaia DR2 color–magnitude diagram of our initial list of MUTA members (red circles), compared with field stars within 100 pc of the Sun (black dots). This list of MUTA members contains several OBA-type stars ($G - G_{\text{RP}} < 0.2$) indicative of its young age, as well as later-type stars ($G - G_{\text{RP}} > 0.2$) that constitute a narrow sequence. The Gaia DR2 photometry was not corrected for interstellar extinction. 2MASS J04212444+0853488 is outside the range of this figure at $G - G_{\text{RP}} = 1.12$. See Section 2 for more details.

kinematic model in UVW space as new candidate members. The latter criterion avoids selecting stars that would fit all BANYAN Σ models poorly, including its model of the local Galactic neighborhood.

These selection criteria resulted in a set of 503 additional candidate members, which are listed in Table 3. Their common proper motion is illustrated in Figure 4, and their positions in a Gaia DR2 $G - G_{\text{RP}}$ color versus absolute G magnitude are shown in Figure 5. Their sky positions are located in the range of 37° – 74° and -4° to $+29^\circ$ in R.A. and decl., and their trigonometric distances are in the range of 100–220 pc, indicating that our initial filtering of Gaia DR2 entries was likely appropriate to encompass the full distribution of MUTA members.

4.1. A Search for Comoving Systems

We complemented our search for MUTA members with a subsequent search for stars comoving with any one of the 540 members and candidate members. All Gaia DR2 entries within 180'' of each MUTA candidate were inspected to find objects comoving within 10 mas yr $^{-1}$ and for which the proper-motion difference is smaller than 5% of the measurement. For most Gaia DR2 entries, a parallax measurement is also available: in these cases, we also required the trigonometric distance of the two objects to be within 5 pc of each other,¹⁰ and we set a maximum parallax difference at 5% of the parallax measurement.

This search identified 26 comoving systems (52 components total) for which both components were already in the list of candidates and two stars (2MASS J03424511+0754507 and 2MASS J02581815+2456552) not already included in our

¹⁰ Throughout this work, we used a parallax zero-point of -0.029 mas (Lindgren et al. 2018) to convert parallaxes to trigonometric distances. We determined trigonometric distances $\varpi = 1/(\pi + 0.029)$, where π is the parallax with a standard error propagation, which is accurate enough for the current purposes given the nearby distances of the stars under consideration.

Table 2
Core Members of MUTA Used in the Construction of a Kinematic Model

MUTA ID	Name	$\mu_{\alpha} \cos \delta$ (mas yr ⁻¹)	μ_{δ} (mas yr ⁻¹)	Parallax (mas)	RV (km s ⁻¹)	RV References
1	μ Eri	13.51 ± 0.75	-13.66 ± 0.64	6.3 ± 0.2	23 ± 4	1
2	μ Tau	20.88 ± 0.62	-22.79 ± 0.52	6.7 ± 0.3	16.3 ± 0.6	1
3 A	30 Tau	25.27 ± 0.28	-23.69 ± 0.23	7.7 ± 0.2	16.2 ± 0.1	1
4	35 Eri	28.45 ± 0.30	-15.28 ± 0.25	7.5 ± 0.2	15.7 ± 0.8	1
5	29 Tau	21.88 ± 0.29	-13.65 ± 0.26	5.3 ± 0.2	17 ± 2	3
6	HD 28375	19.53 ± 0.33	-20.27 ± 0.18	6.8 ± 0.2	18 ± 4	1
7	HD 28843	18.28 ± 0.19	-16.50 ± 0.13	5.9 ± 0.1	18 ± 7	6
8	HD 19698	32.84 ± 0.16	-23.58 ± 0.17	7.4 ± 0.1	1 ± 4	1
9	HR 1307	19.37 ± 0.39	-26.69 ± 0.23	6.9 ± 0.1	10 ± 7	6
10	V766 Tau	23.77 ± 0.11	-23.228 ± 0.079	6.19 ± 0.06	16 ± 2	5
12	HD 24456	26.93 ± 0.10	-20.785 ± 0.074	7.18 ± 0.05	18 ± 3	1
15	HD 25978	18.91 ± 0.16	-22.323 ± 0.076	5.99 ± 0.07	22 ± 7	6
16	HD 26323	22.38 ± 0.12	-20.975 ± 0.071	6.18 ± 0.06	14 ± 3	1
18	HD 28356	20.00 ± 0.15	-21.659 ± 0.072	6.36 ± 0.07	20.6 ± 0.6	2
19 A	HD 23376	26.61 ± 0.11	-24.306 ± 0.066	6.89 ± 0.06	16.5 ± 0.5	2
20	HIP 17133	25.53 ± 0.10	-24.403 ± 0.073	6.63 ± 0.05	14 ± 6	2
21	HD 286374	24.05 ± 0.11	-24.124 ± 0.067	6.54 ± 0.07	14 ± 2	2
22	PPM 119410	24.14 ± 0.10	-24.167 ± 0.068	6.58 ± 0.05	15.0 ± 0.6	2
23	TYC 1248-394-1	24.24 ± 0.14	-21.892 ± 0.072	6.80 ± 0.05	8.0 ± 0.7	4
24	RX J0348.5+0832	25.33 ± 0.11	-22.738 ± 0.070	6.56 ± 0.08	10 ± 10	2
25	TYC 80-202-1	23.547 ± 0.086	-25.480 ± 0.054	5.96 ± 0.05	20.7 ± 0.6	2
26	TYC 662-217-1	24.07 ± 0.11	-25.242 ± 0.063	6.71 ± 0.05	15.3 ± 0.6	2
27	RX J0338.3+1020	26.75 ± 0.10	-24.923 ± 0.070	6.82 ± 0.06	15 ± 1	2
29	RX J0358.2+0932	24.321 ± 0.071	-24.493 ± 0.051	6.78 ± 0.04	16 ± 2	2
30 A	TYC 668-737-1	21.501 ± 0.085	-23.632 ± 0.056	6.57 ± 0.05	20 ± 7	2

Notes. All proper motion and parallax measurements are from Gaia DR2, except for the parallax of μ Eri, which is from Hipparcos (van Leeuwen 2007). See Section 3 for more details.

References. (1) Gontcharov 2006; (2) Gaia Collaboration et al. 2018; (3) Evans 1967; (4) White et al. 2007; (5) Wilson 1953; (6) Kharchenko et al. 2007.

(This table is available in machine-readable form.)

list, each seemingly comoving with a pair of stars in our list of candidates but failing to meet our membership selection criteria (i.e., their Bayesian membership probabilities are 49% and 0%, respectively). In addition to those, we identified 15 systems (21 system components) for which only one component was in our list of candidates because the other component failed to pass our membership selection criteria. All objects were added to our list of low-likelihood candidates for completion, and all comoving systems are listed in Table 4.

One notable case of a star with comoving components is 29 Tau, the most massive member of MUTA. 29 Tau (MUTA 5, Gaia DR2 3276605295710700032) is a B3 + A7 binary star (Beavers & Cook 1980), with three comoving systems within 70'': 29 Tau B (MUTA 139; 2MASS J03454440+0603283; Gaia DR2 3276604922051089664), which is itself a spectral binary (Mason et al. 2001); 29 Tau C (MUTA 137; 2MASS J03454104+0602349; Gaia DR2 3276604544094119424); and 29 Tau D (MUTA 138; 2MASS J03454269+0603039; Gaia DR2 3276604544093968896). In addition to these six system components, there are two other Gaia DR2 entries within $\approx 42''$ of 29 Tau (Gaia DR2 3276604509734231808 and Gaia DR2 3276605265648475776) located within 300 pc of the Sun with inconsistent proper motions and parallaxes. Both of them have renormalized unit weight error (RUWE) values of ≈ 1.1 , which is not clearly indicative of bad parallax solutions and indicates that they are probably unrelated to 29 Tau. For this reason, we ignored them in this analysis, but we would recommend revisiting this when further Gaia data releases are published. Two

additional MUTA candidates are within 700''–715'' of 29 Tau: MUTA 143 (2MASS J03460544+0553074; Gaia DR2 3276586333432639744) and MUTA 135 (2MASS J03450918+0612030; Gaia DR2 3276798401738487808). Gaia DR2 3276584478006772224 also seems comoving with 29 Tau at a separation of 977''.5, but it was not recovered in our search because its MUTA probability (89.7%) is below our selection threshold.

Cross-matching our list of candidates with the Oh et al. (2017) catalog of comoving systems yielded a total of 28 matches, to Groups 39, 43, 52, 60, 124, 242, 1099, and 1109. Each of these groups has a total of members between two and seven. We verified that each of these groups was included in their entirety in our list of MUTA candidates, and we found four missing components of Group 39 and one missing component of Group 1109. We added these objects to our list of low-likelihood MUTA candidates despite their BANYAN Σ membership probabilities below 90% (ranging from 0% to 64%) for completion. As demonstrated by Faherty et al. (2018), the algorithm of Oh et al. (2017) tends to break up nearby associations in many subgroups because of the strong variations and correlations in direct kinematic observables (sky position, proper motion, and parallax) caused by their wide distributions on the sky. The full list of matches between our candidates and Oh et al. (2017) groups is shown in Table 5.

4.2. Red Giant Stars

One candidate member of the MUTA association, HD 27860, is located far above the main sequence and within

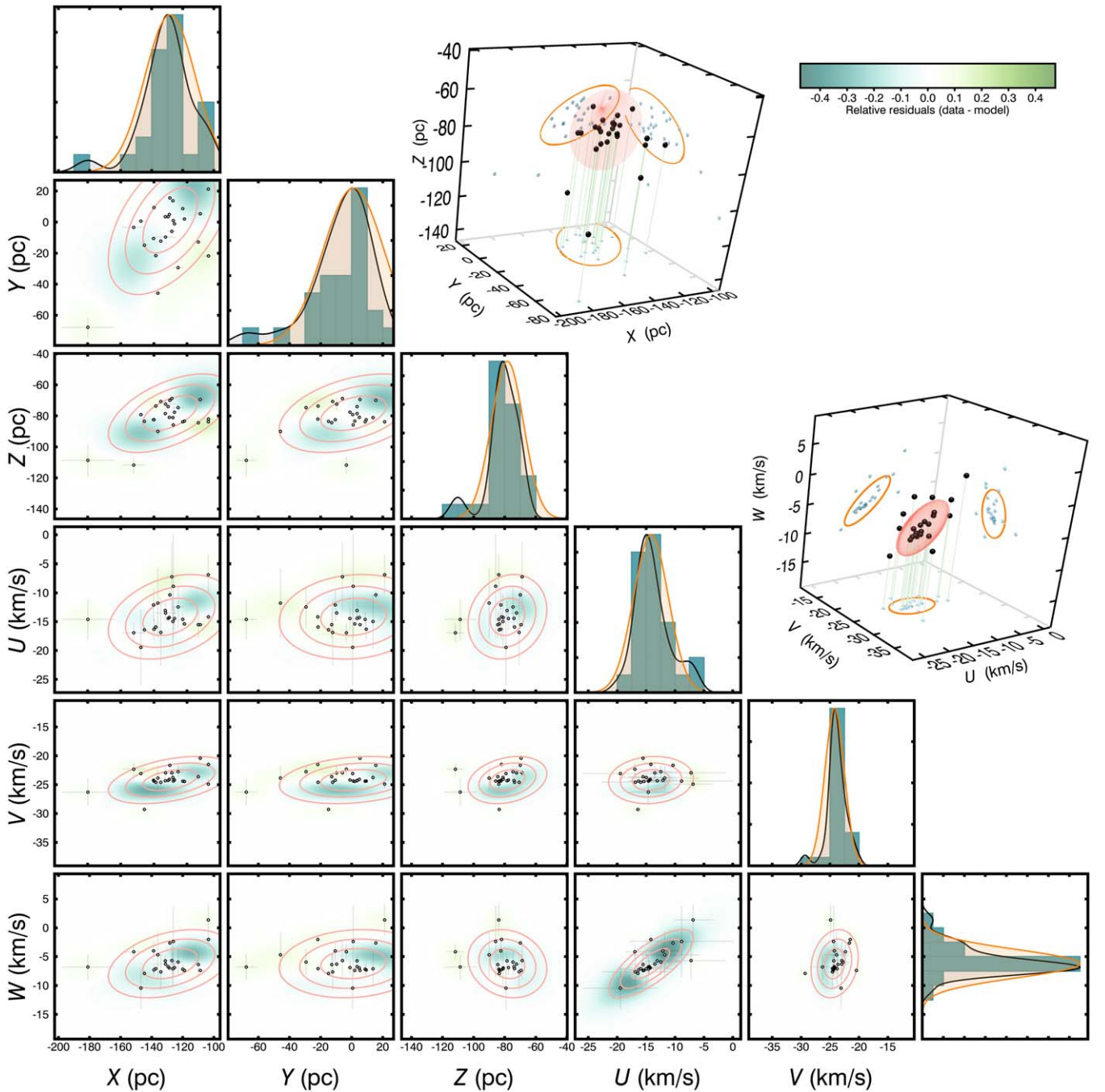


Figure 3. Multivariate Gaussian model of MUTA built for BANYAN Σ . Orange lines show the 1σ , 2σ , and 3σ projected contours of the modeled member distribution, and black points represent individual members. Blue and green shadings represent regions of overdensity (green) and underdensity (blue) of actual members compared to the model and therefore correspond to departures from a multivariate Gaussian distribution. One-dimensional distributions are displayed as green bars and are compared with a kernel density estimate distribution of the members (black line) and the projected model (orange lines). A single 1σ contour (orange surfaces) and individual members (black spheres) with their projections on the three axis planes are shown for the 3D model projections (upper right). See Section 3 for more details.

the red giant branch in Figure 5. A literature search revealed that this object has a spectral type of K2 III (Woolley et al. 1981), consistent with its position in the color–magnitude diagram. Based on the compilations of stars within 40 pc established by Gray et al. (2003, 2006), stars with the same spectral type have an average color $B - V = 1.16$ and absolute magnitude $M_V = 1.3$.¹¹

Using the three-dimensional extinction map SStructuring by Inversion of the Local InterStellar Medium (STILISM; Lallement et al. 2014; Capitanio et al. 2017; Lallement et al. 2018),¹² we can expect HD 27860 to be subject to an extinction $E(B - V) = 0.12 \pm 0.02$ based on its sky position and distance, which translates to $A_V = 0.43 \pm 0.08$ (using a total-to-selective extinction ratio $R = 3.54$ for this photometric

¹¹ See also <http://www.pas.rochester.edu/~emamajek/spt/K2III.txt>.

¹² Available at <https://stilism.obspm.fr>.

Table 3
List of New Candidate Members of MUTA Identified in Gaia DR2 with BANYAN Σ

MUTA ID	Object Name	R.A. (hh:mm:ss.sss)	Decl. (dd:mm:ss.ss)	$\mu_{\alpha} \cos \delta$ (mas yr ⁻¹)	μ_{δ} (mas yr ⁻¹)	Parallax (mas)	RV (km s ⁻¹)	Gaia DR2 (<i>G</i> mag)
31	2MASS J02363660+2026331	02:36:36.648	+20:26:32.84	40.3 ± 1.4	-26.7 ± 1.1	8.82 ± 0.69	...	15.289
32	2MASS J02424085+2558585	02:42:40.905	+25:58:58.08	38.60 ± 0.16	-31.61 ± 0.14	8.80 ± 0.11	...	16.090
33	HD 17008	02:44:30.027	+28:00:53.61	31.19 ± 0.11	-25.95 ± 0.10	7.372 ± 0.066	4 ± 2	7.909
34	2MASS J02484851+1319378	02:48:48.553	+13:19:37.66	34.627 ± 0.062	-23.355 ± 0.054	7.731 ± 0.035	...	14.077
35	TYC 1785-155-1	02:49:43.813	+25:53:11.25	30.146 ± 0.087	-26.174 ± 0.077	7.036 ± 0.044	7.2 ± 0.3	11.679
36	2MASS J02513636+2811000	02:51:36.407	+28:10:59.60	32.002 ± 0.073	-25.265 ± 0.067	7.866 ± 0.036	...	13.629
37	2MASS J02515956+1458162	02:51:59.618	+14:58:15.78	41.0 ± 1.3	-24.72 ± 0.99	8.68 ± 0.78	...	19.815
38	2MASS J02523886+2300093	02:52:38.911	+23:00:08.53	35.50 ± 0.63	-30.31 ± 0.43	8.30 ± 0.32	...	18.548
39	GSC 01230-00749	02:55:04.011	+20:55:18.64	39.250 ± 0.075	-30.957 ± 0.067	7.892 ± 0.043	...	11.948
40	2MASS J02571995+2408232	02:57:19.993	+24:08:22.54	36.577 ± 0.069	-30.638 ± 0.060	7.144 ± 0.038	4 ± 1	12.207
41	TYC 1790-927-1	02:57:43.023	+26:32:03.61	31.150 ± 0.082	-27.362 ± 0.075	7.419 ± 0.043	8 ± 2	11.326
42 B	Gaia DR2 113410746049727744	02:58:16.476	+24:56:42.65	31.83 ± 0.38	-28.33 ± 0.24	6.67 ± 0.23	...	16.776
42 A	2MASS J02581643+2456424	02:58:16.484	+24:56:41.76	31.65 ± 0.33	-27.54 ± 0.26	7.84 ± 0.21	...	15.193

Note. The MUTA identifiers listed in this table are defined in Section 4.4. Some identifiers listed here contain only one component of a binary system (either A or B) because the other component was recovered in either comover searches of Sections 4.1 and 4.4. Only a portion of the table is shown here. The full table is available in a machine-readable format. Targets without a MUTA ID number were flagged as problematic (i.e., low-likelihood candidates). See Section 4 for more details.

(This table is available in its entirety in machine-readable form.)

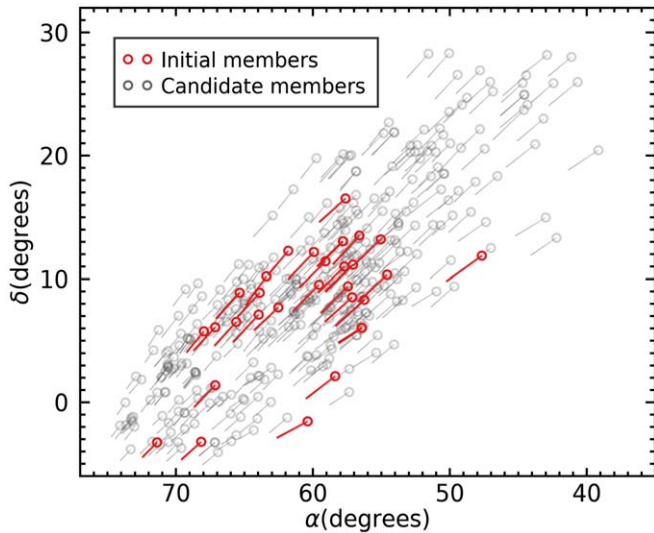


Figure 4. Sky positions and proper-motion vectors for initial members of MUTA (red circles and lines) and additional candidate members recovered in this work (gray circles and lines). See Section 4 for more details.

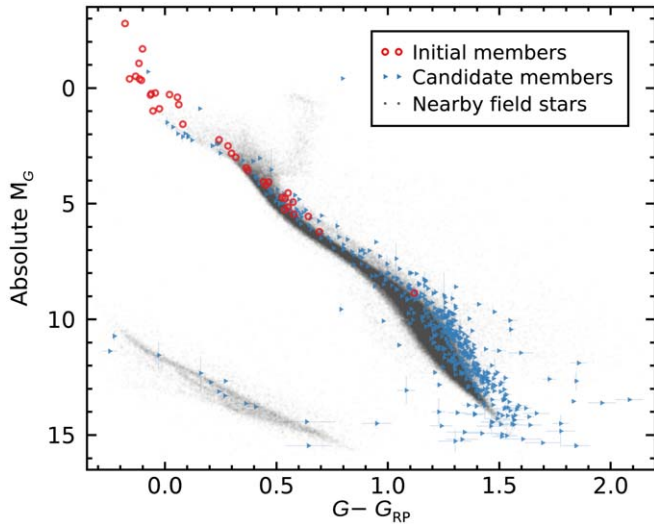


Figure 5. Gaia DR2 color-magnitude diagram of initial MUTA members (red circles) and candidate members (blue rightward-pointing triangles) recovered by BANYAN Σ based on their Gaia DR2 sky positions, proper motions, parallaxes, and radial velocities when available. See Section 4 for more details.

band). Correcting its observed properties in the same photometric bands ($B - V = 1.41 \pm 0.01$ and $M_V = 0.05 \pm 0.02$; ESA 1997) for extinction yields an intrinsic color of $B - V = 1.29 \pm 0.02$ and an absolute magnitude $M_V = -0.38 \pm 0.08$, placing it closer in colors to the average value for K3 III giants ($B - V = 1.37$).

Using the bolometric correction of Flower (1996) for this color ($BC_V = -0.73$), we estimate a bolometric magnitude $M_{\text{bol}} = -1.11 \pm 0.08$ and $\log L/L_{\odot} = 2.36 \pm 0.03$. We estimated its effective temperature at $T_{\text{eff}} \approx 4400$ K by interpolating its extinction-corrected $B - V$ color and comparing them with averages from Gray et al. (2003, 2006) for spectral types K2 III and K3 III. These physical parameters are consistent with a luminosity class of III; the Bertelli et al. (2009) solar-metallicity isochrones predict a mass of $2.44 M_{\odot}$, a surface gravity $\log g \approx 2.0$, and an age of ≈ 650 Myr.

HD 27860 seems significantly too old to be a member of MUTA based on the color-magnitude sequence of this young association (Figure 5). The main-sequence turnoff of a 650 Myr association would be located at spectral types A0 or later¹³ (i.e., at an absolute Gaia DR2 magnitude $M_G \approx 1.5$). The fact that MUTA includes several members more massive than A0 strongly suggests that HD 27860 is a chance interloper despite its high 98.6% Bayesian membership probability, and we therefore reject it from our list of candidate members.

4.3. White Dwarfs

A subset of MUTA members are located below the main sequence and within the color-magnitude sequence of white dwarfs in Figure 2. We flagged all candidates with an absolute G -band magnitude fainter than $(G - G_{\text{RP}}) \cdot 5 + 10$ and a color $G - G_{\text{RP}} < 1.0$ (shown in Figure 6) as likely white dwarfs, and we compared them to total-age isochrones obtained by combining MIST stellar main-sequence lifetimes (Choi et al. 2016) and the Montréal white dwarf cooling tracks (Fontaine et al. 2001),¹⁴ in Figure 7.

All but two white dwarfs in our sample are clearly much older than 150 Myr, inconsistent with the main-sequence turnoff age of MUTA ($\lesssim 80$ Myr). The two youngest and hottest white dwarfs in this figure are WD 0350+098 (MUTA 190; other designations include 1RXS J035315.5+095700, SDSS J035315.72+095633.7) and WD 0340+103 (MUTA 125; other designations include RBS 466, 1RXS J034314.1+102941, and SDSS J034314.35+102938.4) and are discussed further in Section 6.4.

We can estimate a false-positive rate for our list of MUTA candidate members based on the fact that we uncovered 10 white dwarfs that are clearly too old for this young association. The number density of white dwarfs, $(4.49 \pm 0.38) \times 10^{-3}$ objects pc^{-3} (Hollands et al. 2018), is small compared with that of main-sequence stars $(98.4 \pm 6.8) \times 10^{-3}$ objects pc^{-3} ; Kirkpatrick et al. 2012). Assuming that white dwarfs have similar kinematics to main-sequence stars, this means that we could expect as many as 220_{-22}^{+25} stars in our sample to be contaminants if we applied no other cuts than BANYAN Σ probabilities based on proper motion and parallax without radial velocity measurements (none of the white dwarf contaminants have radial velocity measurements). An additional 28 Gaia DR2 sources would have been uncovered in our survey if we used only these observables and no other criteria, leaving our estimated number of contaminants to 192_{-22}^{+25} in our final list of candidates, or $34_{-4}^{+5}\%$ of our full sample of 503 objects. The majority of contaminants are expected to be M dwarfs.

4.4. Poor Astrometric Solutions

The Gaia DR2 team recommends placing low confidence in astrometric solutions with an RUWE larger than 1.4.¹⁵ We therefore flagged all 52 MUTA candidates and members with $\text{RUWE} > 1.4$ (shown in Figure 8) and consider them as low-likelihood candidates; we consider that an observational follow-up of these objects will potentially be useful but should

¹³ See http://www.pas.rochester.edu/~emamajek/EEM_dwarf_UBVIJHK_colors_Teff.txt.

¹⁴ Available at <http://www.astro.umontreal.ca/~bergeron/CoolingModels/>; see also Holberg & Bergeron (2006), Kowalski & Saumon (2006), Tremblay et al. (2011), and Bergeron et al. (2011).

¹⁵ As described at <https://www.cosmos.esa.int/web/gaia/dr2-known-issues>.

Table 4
Wide Multiple Systems Recovered in MUTA

MUTA ID	Name	R.A. (hh:mm:ss.sss)	Decl. (dd:mm:ss.ss)	$\mu_{\alpha} \cos \delta$ (mas yr ⁻¹)	μ_{δ} (mas yr ⁻¹)	Parallax (mas)	Gaia DR2 <i>G</i> mag	Sep. (arcsec)	Pos. Ang. (deg)
5	29 Tau	03:45:40.466	+06:02:59.78	21.88 ± 0.29	-13.65 ± 0.26	5.3 ± 0.2	5.295 ± 0.001
137	2MASS J03454104+0602349	03:45:41.066	+06:02:34.59	21.27 ± 0.21	-14.11 ± 0.17	5.5 ± 0.1	16.660 ± 0.002	26.7278 ± 0.0001	160.4167 ± 0.0004
138	2MASS J03454269+0603039	03:45:42.712	+06:03:03.66	21.11 ± 0.12	-13.801 ± 0.091	5.55 ± 0.07	15.389 ± 0.001	33.7294 ± 0.0002	83.3927 ± 0.0002
139	2MASS J03454440+0603283	03:45:44.425	+06:03:28.04	19.950 ± 0.077	-13.189 ± 0.053	5.56 ± 0.05	12.3683 ± 0.0004	65.4671 ± 0.0002	64.4250 ± 0.0001
10	V766 Tau	03:51:15.896	+13:02:45.52	23.77 ± 0.11	-23.228 ± 0.079	6.19 ± 0.06	6.247 ± 0.001
182	2MASS J03511041+1302467	03:51:10.454	+13:02:46.16	23.10 ± 0.17	-23.14 ± 0.12	6.1 ± 0.1	16.117 ± 0.001	79.5332 ± 0.0001	270.4681 ± 0.0001
19 A	HD 23376	03:44:58.957	+08:19:10.09	26.61 ± 0.11	-24.306 ± 0.066	6.89 ± 0.06	9.2549 ± 0.0003
19 B	TYC 658-1007-2	03:44:59.048	+08:19:13.81	26.577 ± 0.099	-24.198 ± 0.062	6.99 ± 0.07	10.493 ± 0.002	3.9534 ± 0.0001	19.894 ± 0.001
30 A	TYC 668-737-1	04:21:24.386	+08:53:54.34	21.501 ± 0.085	-23.632 ± 0.056	6.57 ± 0.05	11.356 ± 0.002
30 B	2MASS J04212444+0853488	04:21:24.473	+08:53:48.52	21.62 ± 0.10	-23.778 ± 0.064	6.59 ± 0.06	14.7603 ± 0.0007	5.9608 ± 0.0001	167.5144 ± 0.0006
42 A	2MASS J02581643+2456424	02:58:16.484	+24:56:41.76	31.65 ± 0.33	-27.54 ± 0.26	7.84 ± 0.21	15.193
42 B	Gaia DR2 113410746049727744	02:58:16.476	+24:56:42.65	31.83 ± 0.38	-28.33 ± 0.24	6.67 ± 0.23	16.776	0.9011 ± 0.0002	353.00 ± 0.02
373	2MASS J02581815+2456552	02:58:18.198	+24:56:54.67	24.1 ± 1.5	-33.7 ± 1.3	6.9 ± 1.2	20.136	26.6513 ± 0.0009	61.016 ± 0.002
130 A	2MASS J03442859+0716100	03:44:28.602	+07:16:10.10	25.80 ± 0.18	-22.56 ± 0.15	6.6 ± 0.1	16.3270 ± 0.0007
130 B	Gaia DR2 3277686910210391424	03:44:28.657	+07:16:08.46	24.39 ± 0.21	-23.66 ± 0.17	6.7 ± 0.1	16.596 ± 0.001	1.8368 ± 0.0001	153.315 ± 0.004
144 A	2MASS J03463553+1317056	03:46:35.533	+13:17:06.31	22.17 ± 0.26	-24.02 ± 0.17	6.3 ± 0.1	17.335 ± 0.002
144 B	Gaia DR2 37943944413361792	03:46:35.594	+13:17:04.31	23.04 ± 0.30	-24.20 ± 0.20	6.5 ± 0.2	17.365 ± 0.002	2.1835 ± 0.0001	156.243 ± 0.005
149	2MASS J03471144+0526234	03:47:11.466	+05:26:23.15	22.84 ± 0.12	-19.71 ± 0.10	6.09 ± 0.07	14.6109 ± 0.0005	31.1351 ± 0.0001	269.3679 ± 0.0001
150	BD+04 589	03:47:13.551	+05:26:23.49	22.654 ± 0.098	-17.159 ± 0.084	5.86 ± 0.05	9.3101 ± 0.0003
159	TYC 71-542-1	03:47:56.865	+06:16:06.67	21.191 ± 0.082	-13.396 ± 0.055	5.40 ± 0.04	11.164 ± 0.002
374	2MASS J03475024+0617499	03:47:50.279	+06:17:49.65	20.96 ± 0.18	-13.27 ± 0.13	5.42 ± 0.09	16.910 ± 0.001	142.3001 ± 0.0001	316.3645 ± 0.0001
188 A	2MASS J03524018+0830333	03:52:40.220	+08:30:33.13	21.96 ± 0.17	-22.24 ± 0.11	5.46 ± 0.08	16.0063 ± 0.0008
188 B	Gaia DR2 3301507795268229248	03:52:40.165	+08:30:30.19	21.32 ± 0.38	-21.97 ± 0.25	5.5 ± 0.2	17.668 ± 0.001	3.0421 ± 0.0001	195.371 ± 0.003
231 A	2MASS J04044937+0935076	04:04:49.382	+09:35:07.13	22.40 ± 0.18	-24.31 ± 0.11	6.6 ± 0.1	15.4101 ± 0.0007
231 B	Gaia DR2 3301900595795159040	04:04:49.493	+09:35:07.71	24.12 ± 0.28	-23.21 ± 0.17	6.9 ± 0.2	16.845 ± 0.002	1.7370 ± 0.0002	70.514 ± 0.003
236 A	2MASS J04054018+0722109	04:05:40.210	+07:22:10.83	20.45 ± 0.35	-18.09 ± 0.20	4.7 ± 0.2	17.633 ± 0.001
236 B	Gaia DR2 3297969498128206208	04:05:40.167	+07:22:12.08	19.0 ± 1.9	-17.24 ± 0.93	4.7 ± 0.8	20.068 ± 0.005	1.3996 ± 0.0005	333.19 ± 0.03
265 A	2MASS J04161320-0119554	04:16:13.253	-01:19:55.93	21.61 ± 0.13	-19.673 ± 0.098	7.20 ± 0.08	15.205 ± 0.001
265 B	Gaia DR2 3254162137382331136	04:16:13.147	-01:19:54.96	22.95 ± 0.15	-18.42 ± 0.14	6.86 ± 0.09	16.068 ± 0.002	1.8653 ± 0.0001	301.262 ± 0.003
267	UCAC2 30946195	04:17:18.672	-02:16:02.15	19.267 ± 0.047	-11.584 ± 0.022	5.64 ± 0.04	11.4912 ± 0.0009	26.7762 ± 0.0001	25.0444 ± 0.0001
375	HD 27162	04:17:17.915	-02:16:26.41	19.235 ± 0.083	-11.433 ± 0.039	5.70 ± 0.06	8.3164 ± 0.0003
287 A	2MASS J04200281+0010109	04:20:02.840	+00:10:10.78	16.170 ± 0.070	-15.678 ± 0.042	4.43 ± 0.04	15.0711 ± 0.0004
287 B	Gaia DR2 3254797311502540032	04:20:02.874	+00:10:08.62	17.18 ± 0.70	-15.91 ± 0.46	4.6 ± 0.5	19.318 ± 0.004	2.2205 ± 0.0003	166.80 ± 0.01
280 A	CRTS J042024.3+001725	04:20:24.319	+00:17:25.43	18.484 ± 0.037	-12.270 ± 0.024	5.61 ± 0.03	13.280 ± 0.002
280 B	Gaia DR2 3254823940299749376	04:20:24.331	+00:17:26.71	19.99 ± 0.28	-11.05 ± 0.16	5.6 ± 0.2	16.220 ± 0.002	1.2880 ± 0.0001	7.395 ± 0.007
305 A	BD-03 789	04:28:37.716	-03:15:44.58	21.005 ± 0.058	-18.285 ± 0.043	6.72 ± 0.04	9.9877 ± 0.0007
305 B	2MASS J04283839-0315371	04:28:38.423	-03:15:37.42	21.409 ± 0.061	-17.884 ± 0.045	6.78 ± 0.05	14.304 ± 0.002	12.7788 ± 0.0001	55.9407 ± 0.0002

Table 4
(Continued)

MUTA ID	Name	R.A. (hh:mm:ss.sss)	Decl. (dd:mm:ss.ss)	$\mu_{\alpha} \cos \delta$ (mas yr ⁻¹)	μ_{δ} (mas yr ⁻¹)	Parallax (mas)	Gaia DR2 <i>G</i> mag	Sep. (arcsec)	Pos. Ang. (deg)
324 A	HD 29182	04:35:53.776	+05:06:15.36	13.562 ± 0.084	-18.825 ± 0.051	5.50 ± 0.05	8.6917 ± 0.0002
324 B	TYC 90-953-1	04:35:52.439	+05:05:30.40	14.070 ± 0.062	-18.775 ± 0.037	5.58 ± 0.04	11.4861 ± 0.0009	49.1962 ± 0.0001	203.9532 ± 0.0001
325 A	2MASS J04363330+0511304	04:36:33.328	+05:11:29.84	15.123 ± 0.081	-19.524 ± 0.050	5.63 ± 0.05	14.831 ± 0.001
325 B	Gaia DR2 3282460371222713728	04:36:33.274	+05:11:31.41	14.77 ± 0.14	-19.544 ± 0.089	5.71 ± 0.09	16.270 ± 0.001	1.7658 ± 0.0001	333.156 ± 0.002
338 A	TYC 4739-1225-1	04:39:20.251	-03:14:21.79	14.784 ± 0.080	-16.007 ± 0.056	6.09 ± 0.04	10.9621 ± 0.0008
338 B	2MASS J04392073-0314301	04:39:20.752	-03:14:30.44	15.80 ± 0.13	-15.330 ± 0.095	6.21 ± 0.06	14.3892 ± 0.0005	11.4482 ± 0.0001	139.0309 ± 0.0003
346 A	2MASS J04421498+0250387	04:42:14.998	+02:50:38.54	14.310 ± 0.082	-17.815 ± 0.056	5.82 ± 0.05	14.8299 ± 0.0008
346 B	2MASS J04421451+0250336	04:42:14.531	+02:50:33.42	14.70 ± 0.23	-16.73 ± 0.18	5.8 ± 0.1	17.743 ± 0.001	8.6712 ± 0.0001	233.8027 ± 0.0006
351	TYC 83-1232-1	04:43:04.063	+00:49:47.45	14.188 ± 0.095	-17.190 ± 0.058	5.81 ± 0.05	11.189 ± 0.002
353	2MASS J04431309+0048174	04:43:13.116	+00:48:17.19	13.76 ± 0.14	-16.967 ± 0.083	5.79 ± 0.08	14.479 ± 0.001	163.0508 ± 0.0001	123.6116 ± 0.0001
371 A	2MASS J04544679-0001085	04:54:46.790	-00:01:08.42	10.897 ± 0.033	-15.313 ± 0.027	5.40 ± 0.02	13.325 ± 0.002
371 B	Gaia DR2 3228318975563766784	04:54:46.875	-00:01:10.21	11.191 ± 0.065	-16.437 ± 0.050	5.32 ± 0.04	14.858 ± 0.001	2.1970 ± 0.0001	144.7240 ± 0.0009
372 A	TYC 4741-307-1	04:56:18.287	-01:53:33.04	11.95 ± 0.12	-15.188 ± 0.075	5.61 ± 0.06	10.775 ± 0.001
372 B	2MASS J04561830-0153393	04:56:18.315	-01:53:39.53	12.59 ± 0.16	-14.91 ± 0.10	5.62 ± 0.07	15.877 ± 0.001	6.5078 ± 0.0001	176.3739 ± 0.0008
...	2MASS J03250457+0728193	03:25:04.592	+07:28:18.82	31.22 ± 0.26	-21.79 ± 0.20	6.8 ± 0.2	17.360 ± 0.002
...	Gaia DR2 9977797439144320	03:25:04.736	+07:28:20.43	31.93 ± 0.38	-21.57 ± 0.31	6.8 ± 0.3	18.012 ± 0.003	2.6658 ± 0.0002	53.045 ± 0.004
...	HD 23110	03:42:45.949	+07:54:10.34	33.89 ± 0.26	-18.72 ± 0.23	7.8 ± 0.1	7.7818 ± 0.0004
...	TYC 657-794-2	03:42:46.021	+07:54:09.49	35.75 ± 0.65	-9.83 ± 0.69	7.5 ± 0.2	10.038 ± 0.005	1.3660 ± 0.0002	128.34 ± 0.01
...	2MASS J03424511+0754507	03:42:45.157	+07:54:50.35	31.74 ± 0.28	-18.06 ± 0.20	7.9 ± 0.1	17.864 ± 0.002	41.7030 ± 0.0001	343.5988 ± 0.0002

Note. See Section 4.1 for more details.

(This table is available in machine-readable form.)

Table 5
MUTA Objects in Common with Oh et al. (2017)

MUTA ID	Name	Gaia DR2 ID	Oh et al. (2017) Group	Object Type ^a
368	HD 31125	3226496187146449920	39	Candidates
369	TYC 4745–475–1	3224698799168916864	39	Candidates
372 A	TYC 4741–307–1	3225639289631939456	39	Candidates
379	BD+00 884	3231439080323844864	39	Incomplete
380	HD 32264	3225291882613467520	39	Incomplete
381	HD 32721	3212973572810773120	39	Incomplete
382	HD 33023	3212956839618107648	39	Incomplete
10	V766 Tau	37136834159399808	43	Initial
21	HD 286374	3303308245556503296	43	Initial
22	PPM 119410	36595943156045824	43	Initial
26	TYC 662–217–1	3304906145189468416	43	Initial
28	TYC 664–136–1	39841357885932288	43	Initial
377	HIP 18778	3301831773241303552	43	Initial
13	HD 23990	3302396166303947904	52	Initial
19 A	HD 23376	3278197770802258944	52	Initial
19 B	TYC 658–1007–2	3278197766505583232	52	Initial
95	HD 22073	11397988505713536	52	Candidates
140	TYC 658–828–1	3278300987456845440	52	Candidates
17	HD 27687	3286590824092307200	60	Initial
18	HD 28356	3285720938596464640	60	Initial
25	TYC 80–202–1	3297372944352021120	60	Initial
30 A	TYC 668–737–1	3299167141170181888	60	Initial
290	BD+05 638	3284966433101477376	60	Candidates
33	HD 17008	127148009968227584	124	Candidates
35	TYC 1785–155–1	114510012864474112	124	Candidates
41	TYC 1790–927–1	115353480017970560	124	Candidates
11	HD 28715	3285542336676520448	242	Initial
324 A	HD 29182	3282435563491664896	242	Candidates
324 B	TYC 90–953–1	3282434979377650176	242	Incomplete
20	HIP 17133	38088873789758720	1099	Initial
117 A	TYC 663–362–1	38076641722829440	1099	Candidates
376	TYC 665–150–1	38398936068862464	1109	Candidates
378	HD 286412	3305439511410844800	1109	Incomplete

Notes. See Section 4.1 for more details

^a Initial: members of MUTA from our initial list. Candidates: candidates of MUTA recovered in Section 4. Incomplete: targets missing from our list of MUTA initial members and new candidates.

(This table is available in machine-readable form.)

be less of a priority. It is likely that some of these issues will be resolved in the next Gaia data release.

4.5. Visual Inspection of Finder Charts

We generated finder charts for all MUTA objects with available survey data from DSS, SDSS (Alam et al. 2015), UKIDSS (Lawrence et al. 2007), VHS (McMahon et al. 2013), Pan-STARRS (Chambers et al. 2016), WISE (Wright et al. 2010), and 2MASS (Skrutskie et al. 2006) with the `finder_charts.py` Python package (Gagné et al. 2018e),¹⁶ on which we overlaid Gaia DR2 catalog entries, with arrows and symbol sizes indicating their individual proper motions and distances. We used these figures to identify and correct any mismatches in our automated cross-matches to 2MASS and WISE, which tends to happen when a target has a missing entry in either catalog.

We also verified that binaries and comoving systems had the correct component attached to each catalog, and we noted 12 stars that visually appeared comoving with one of our targets at a

similar distance but were not recovered with our comoving search described in Section 4.1. Those usually have Gaia DR2 proper motions or parallaxes that are slight mismatches to our MUTA candidate or member and are listed in Table 6. It is possible that some of these systems suffer from a bad parallax solution, either because they are themselves multiple systems (e.g., 30 Tau and TYC 661–1404–1, respectively, MUTA 3 A and MUTA 3 B) or because they are contaminated by a background source (although they all have $\text{RUWE} \leq 1.4$). We listed these systems that almost seem comoving in Table 6 for later follow-up, but we excluded them from the current analysis.

A number of MUTA candidates are located well below the main sequence in a Gaia DR2 color–magnitude diagram (see Figure 5) but are not faint enough to be credible white dwarfs (see Section 4.3). A fraction of these objects failed the Gaia DR2 $\text{RUWE} \leq 1.4$ selection criterion for good astrometric solutions, indicating that bad parallax solutions are likely part of the explanation. Figure 9 shows a finder chart for one such object (WISEA J033742.99+191646.7).¹⁷ In this example, the finder chart shows that it is well detected at red–optical

¹⁶ Available at https://github.com/jgagneastro/finder_charts.

¹⁷ All finder charts are available as online-only supplementary data.

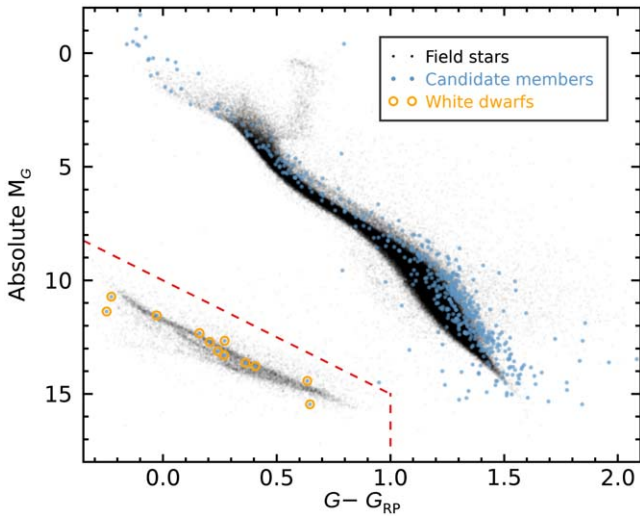


Figure 6. Selection criterion for white dwarfs based on Gaia DR2 color-magnitude positions. See Section 4.3 for more details.

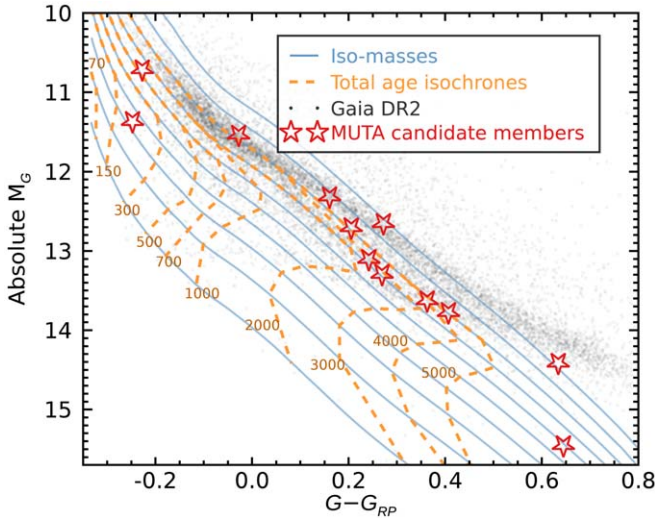


Figure 7. MUTA candidates recovered in Gaia DR2 data whose color-magnitude positions are consistent with white dwarfs (red star symbols). Nearby white dwarfs in Gaia DR2 are indicated with black dots, and total-age isochrones from 70 Myr to 5 Gyr are indicated with orange dashed lines. Iso-masses from $0.4 M_{\odot}$ (top) to $1.3 M_{\odot}$ (bottom) by steps of $0.1 M_{\odot}$ are displayed with blue lines. Most white dwarfs recovered here are too old to be coeval with MUTA. No correction for interstellar extinction was applied in this figure. See Section 4.3 for more details.

wavelengths (e.g., Pan-STARRS) and in WISE W1, but too faint to be detected in 2MASS in the near-infrared. This unusual combination indicates a likely contribution from two distinct blackbodies. The presence of an accretion disk could potentially explain this; however, those usually result in much redder Gaia DR2 $G - G_{RP}$ colors, which would push the object far to the right of, rather than below, the main sequence. The simplest explanation seems to be that this object is a blend of two sources, maybe located at different distances, but at an angular separation small enough that they are unresolved in all the aforementioned surveys.

We assigned MUTA identifiers (31 to 372) to all candidate members that were not rejected or defined as low-likelihood candidates based on their poor astrometric solutions, ages

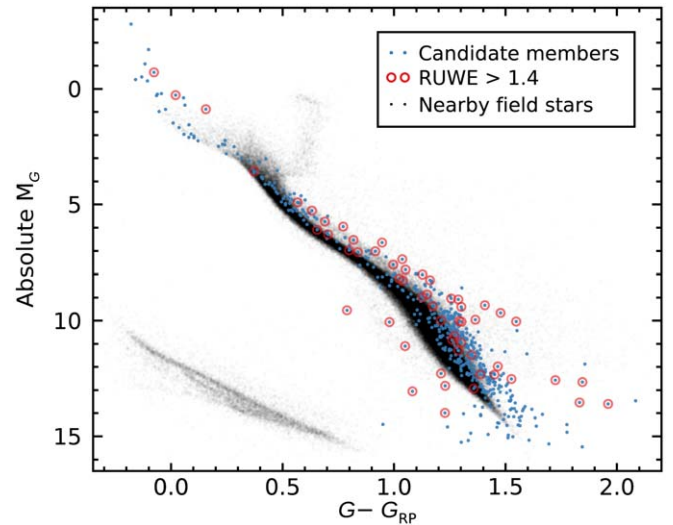


Figure 8. Gaia DR2 color-magnitude diagram of MUTA members and candidates (red circles) compared with nearby field stars (black circles). All objects flagged as problematic because of their poor Gaia DR2 astrometric solutions ($\text{RUWE} > 1.4$) are marked with red circles. A large fraction of these problematic solutions are located below the sequence of members, likely because of contamination by an unresolved source, or consist of possible multiple systems located above the MUTA sequence. See Section 4.4 for more details.

that are definitely too old, or a problematic position in a color-magnitude diagram. We ordered these identifiers by R.A. Stars identified in Section 4.1 as comoving with a well-behaved MUTA candidate or member that did not have a MUTA identifier were assigned identifiers 373–375. Those still without identifiers that belong in one of the Oh et al. (2017) groups associated with MUTA were assigned identifiers 376–382, and those visually identified as comoving with a well-behaved candidate in this section were assigned identifiers 383–386.

5. Correcting Extinction in Gaia DR2 Photometry

The MUTA association is distant enough that some of its members appear slightly reddened by interstellar dust. We used STILISM (Lallement et al. 2014; Capitanio et al. 2017; Lallement et al. 2018)¹⁸ to determine the individual $E(B - V)$ extinction values for individual MUTA objects based on their sky position and Gaia DR2 distance. The resulting individual extinction values are displayed in Figure 10.

We corrected the color-magnitude diagram position of MUTA members and candidates with an iterative method to account for the wide Gaia DR2 photometric bandpasses. As shown in Figure 11, even the G_{RP} bandpass spans a significant region over which both the extinction curve of Fitzpatrick (1999) and the spectral energy density of an M-type star vary significantly. As a consequence, the reddening vectors in Gaia DR2 color-magnitude sequences will differ significantly across spectral types.

¹⁸ Available at <https://stilism.obspm.fr>.

Table 6
Wide Multiple Candidate Systems in MUTA Visually Identified but Not Recovered in Section 4.1

MUTA ID	Name	R.A. (hh:mm:ss.sss)	Decl. (dd:mm:ss.ss)	$\mu_{\alpha} \cos \delta$ (mas yr ⁻¹)	μ_{δ} (mas yr ⁻¹)	Parallax (mas)	Gaia DR2 G mag	Sep. (arcsec)	Pos. Ang. (deg)
3 A	30 Tau	03:48:16.292	+11:08:35.52	25.27 ± 0.28	-23.69 ± 0.23	7.74 ± 0.17	5.040
3 B	TYC 661-1404-1	03:48:16.835	+11:08:40.16	25.62 ± 0.15	-24.97 ± 0.11	7.223 ± 0.070	9.269	9.2389 ± 0.0001	59.8505 ± 0.0007
5	29 Tau	03:45:40.466	+06:02:59.78	21.88 ± 0.29	-13.65 ± 0.26	5.31 ± 0.25	5.295
383	2MASS J03453759+0603048	03:45:37.587	+06:03:04.31	-1.86 ± 0.11	-25.471 ± 0.085	5.427 ± 0.070	15.481	43.1779 ± 0.0002	276.0326 ± 0.0001
97 A	2MASS J03350340+1431490	03:35:03.438	+14:31:48.54	26.99 ± 0.14	-25.93 ± 0.11	7.342 ± 0.081	15.369
97 B	2MASS J03350317+1431358	03:35:03.209	+14:31:35.33	26.87 ± 0.39	-25.57 ± 0.30	6.84 ± 0.24	18.097	13.6275 ± 0.0002	194.1236 ± 0.0008
104 A	2MASS J03361762+2153391	03:36:17.665	+21:53:38.50	29.492 ± 0.088	-30.262 ± 0.068	7.526 ± 0.047	10.910
104 B	2MASS J03361732+2153271	03:36:17.360	+21:53:26.42	29.95 ± 0.71	-31.17 ± 0.52	7.98 ± 0.31	18.454	12.8056 ± 0.0002	199.354 ± 0.002
117 A	TYC 663-362-1	03:40:57.781	+13:09:03.06	24.66 ± 0.25	-25.44 ± 0.21	6.749 ± 0.098	10.493
117 B	2MASS J03405723+1308577	03:40:57.261	+13:08:57.23	27.03 ± 0.71	-24.78 ± 0.50	7.19 ± 0.33	18.437	9.5851 ± 0.0003	232.539 ± 0.002
153 A	TYC 1252-301-1	03:47:23.901	+18:43:17.68	21.128 ± 0.079	-23.175 ± 0.057	5.926 ± 0.041	11.689
153 B	Gaia DR2 44752086050666368	03:47:23.645	+18:43:18.70	21.33 ± 0.60	-26.33 ± 0.57	6.36 ± 0.34	17.855	3.7781 ± 0.0003	285.639 ± 0.004
177 A	2MASS J03505694+0730565	03:50:56.976	+07:30:56.18	30.41 ± 0.23	-22.22 ± 0.16	8.29 ± 0.12	16.916
177 B	Gaia DR2 3277369048270999936	03:50:56.968	+07:30:53.92	27.9 ± 2.2	-21.7 ± 1.4	6.3 ± 1.3	20.438	2.2609 ± 0.0005	183.03 ± 0.03
225 A	2MASS J04021281+0817400	04:02:12.839	+08:17:39.75	23.38 ± 0.24	-22.68 ± 0.17	6.62 ± 0.13	16.635
225 B	2MASS J04021257+0817410	04:02:12.593	+08:17:40.67	22.00 ± 0.36	-23.46 ± 0.25	6.19 ± 0.19	17.316	3.7653 ± 0.0002	284.200 ± 0.002
271	2MASS J04181095+0934586	04:18:10.980	+09:34:58.24	15.97 ± 0.27	-21.58 ± 0.21	5.83 ± 0.16	17.228	26.4111 ± 0.0001	326.8006 ± 0.0003
384	2MASS J04181193+0934365	04:18:11.958	+09:34:36.14	19.11 ± 0.19	-21.51 ± 0.14	4.74 ± 0.11	16.800
277 A	2MASS J04200165+0759584	04:20:01.666	+07:59:57.72	22.83 ± 0.68	-23.94 ± 0.47	6.31 ± 0.34	15.336
277 B	Gaia DR2 3298956138016754048	04:20:01.719	+07:59:58.51	19.87 ± 0.90	-21.65 ± 0.42	6.69 ± 0.14	16.289	1.1173 ± 0.0003	44.75 ± 0.02
279	2MASS J04201617+0959534	04:20:16.202	+09:59:53.06	17.34 ± 0.38	-20.97 ± 0.19	6.14 ± 0.17	17.379	7.1832 ± 0.0001	18.446 ± 0.001
385	TYC 671-129-1	04:20:16.048	+09:59:46.25	16.91 ± 0.14	-22.140 ± 0.066	5.668 ± 0.061	10.795
318 A	2MASS J04341953+0226260	04:34:19.560	+02:26:25.89	16.32 ± 0.42	-20.02 ± 0.29	5.77 ± 0.22	12.150
318 B	Gaia DR2 3279527149078835712	04:34:19.467	+02:26:25.91	15.62 ± 0.75	-21.63 ± 0.44	6.24 ± 0.33	15.960	1.4009 ± 0.0003	270.61 ± 0.01
329 A	2MASS J04372971-0051241	04:37:29.730	-00:51:24.47	15.026 ± 0.042	-16.665 ± 0.027	6.050 ± 0.025	13.223
329 B	Gaia DR2 3229491776511286016	04:37:29.780	-00:51:25.66	14.70 ± 0.36	-17.42 ± 0.19	5.75 ± 0.14	16.507	1.4169 ± 0.0001	147.563 ± 0.006
331 A	2MASS J04382750-0342441	04:38:27.523	-03:42:44.47	23.399 ± 0.072	-20.462 ± 0.051	6.076 ± 0.041	14.931
331 B	Gaia DR2 3201810884087980800	04:38:27.437	-03:42:46.23	19.59 ± 0.85	-17.76 ± 0.49	6.77 ± 0.40	18.416	2.1809 ± 0.0003	216.359 ± 0.007
368	HD 31125	04:53:04.828	-01:16:33.04	12.67 ± 0.11	-15.782 ± 0.072	5.644 ± 0.051	7.918
386	HD 31124	04:53:04.574	-01:15:52.17	19.54 ± 0.19	-17.88 ± 0.12	6.081 ± 0.098	8.046	41.0425 ± 0.0001	354.6787 ± 0.0001
...	2MASS J03343284+1212290	03:34:32.872	+12:12:28.55	27.892 ± 0.090	-30.240 ± 0.063	6.740 ± 0.044	12.302
...	Gaia DR2 40541334474313728	03:34:33.106	+12:12:29.76	28.23 ± 0.88	-29.63 ± 0.62	7.50 ± 0.54	19.087	3.6272 ± 0.0004	70.436 ± 0.005

Note. See Section 4.5 for more details.

(This table is available in machine-readable form.)

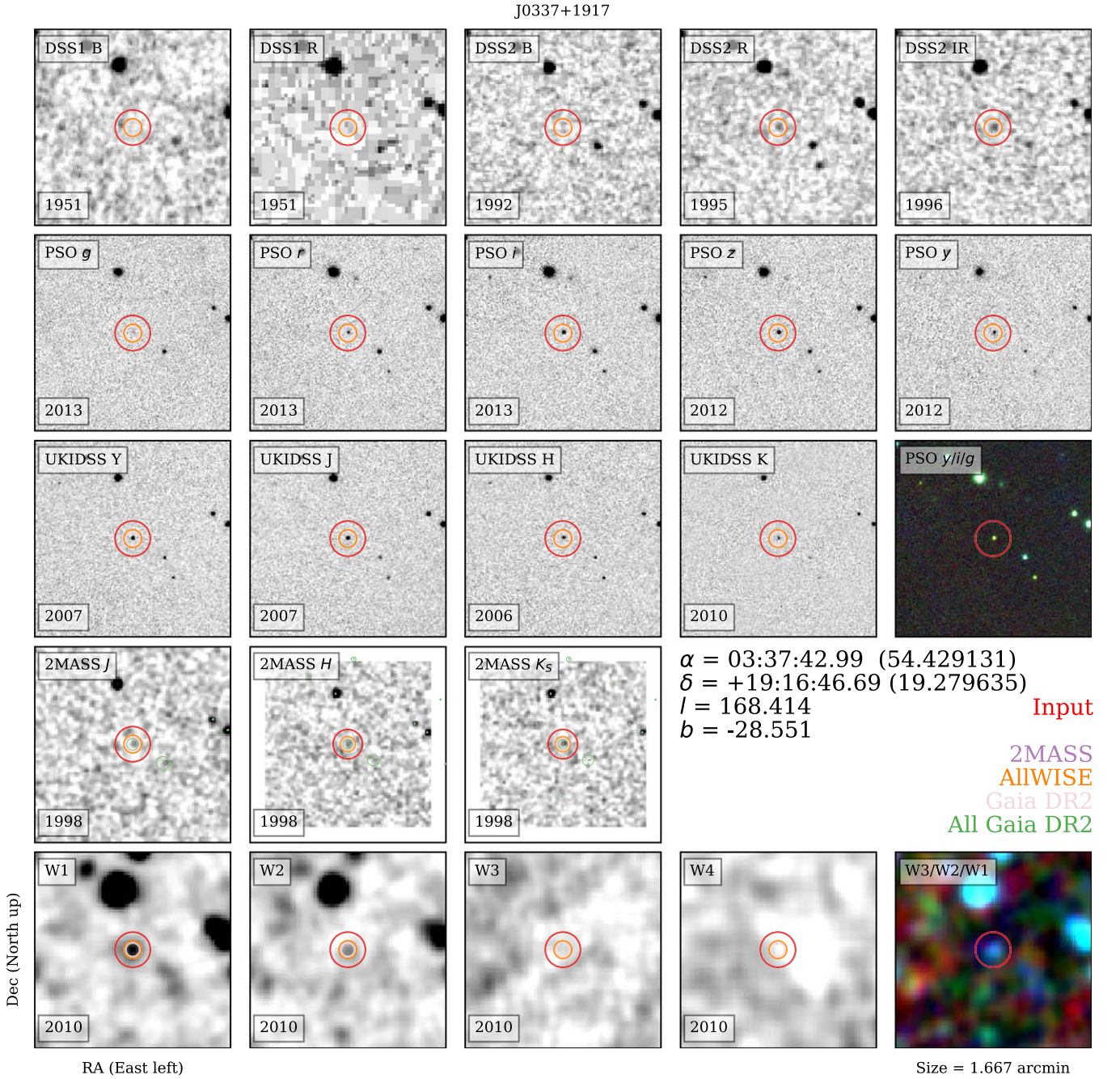


Figure 9. Finder charts for WISEA J033742.99+191646.7, a problematic candidate because its position in a Gaia DR2 color–magnitude diagram is well below the main sequence, likely because of contamination from a background source at a very small angular separation. Finder charts for the other 566 MUTA candidates are also available online as a figure set. See Section 4.5 for more details.

(The complete figure set (566 images) is available.)

The flux of a star with a spectral energy density S_λ observed through an instrument with a bandpass P_λ is given by

$$F = \frac{\int_0^\infty S_\lambda P_\lambda d\lambda}{\int_0^\infty P_\lambda d\lambda}. \quad (1)$$

In the presence of interstellar extinction E_λ , the observed flux is

$$F_{\text{reddened}} = \frac{\int_0^\infty E_\lambda S_\lambda P_\lambda d\lambda}{\int_0^\infty P_\lambda d\lambda}, \quad (2)$$

and therefore the correction factor that remains valid for wide bandpasses is

$$\frac{F_{\text{reddened}}}{F} = \frac{\int_0^\infty E_\lambda S_\lambda P_\lambda d\lambda}{\int_0^\infty S_\lambda P_\lambda d\lambda}. \quad (3)$$

In effect, this correction is a weighted average of the extinction curve, where the weight is given by the product of the stellar spectral energy density with the instrumental bandpass. In general, the spectral energy densities of MUTA members and candidates have not been measured, and their

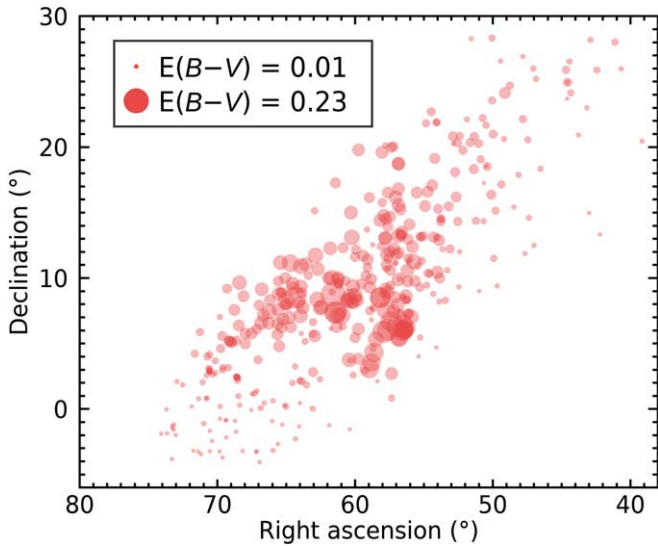


Figure 10. Individual $E(B - V)$ extinctions of MUTA objects based on the STILISM three-dimensional extinction map combined with the sky positions and Gaia DR2 distances of MUTA objects. See Section 5 for more details.

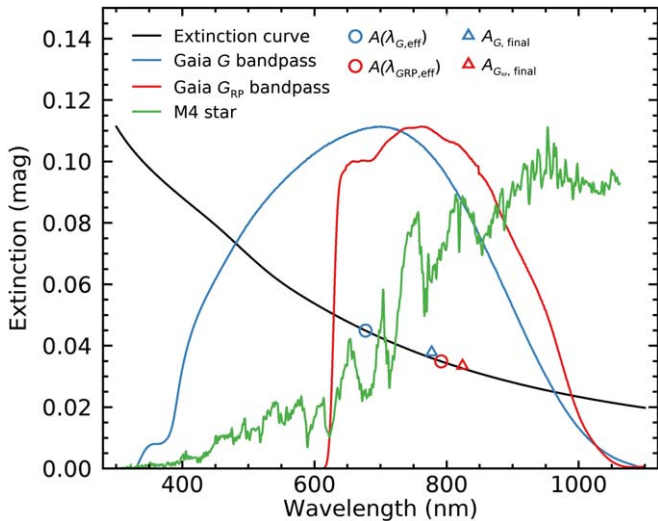


Figure 11. Fitzpatrick (1999) interstellar extinction curve (black line) compared with Gaia DR2 G and $G - G_{\text{RP}}$ bandpasses (blue and red, respectively) and the spectral flux density of an M4 low-mass star (green). Using only the effective wavelength of Gaia DR2 bandpasses to estimate extinction (blue and red circles) leads to an overestimation of dereddening and a mistaken reddening vector angle compared with a more careful extinction correction that accounts for the stellar flux across the Gaia DR2 bandpasses (blue and red triangles). This effect is highly dependent on the spectral type of the star because of the wide Gaia DR2 bandpasses. See Section 5 for more details.

spectral types are unknown. We therefore used an iterative method where the photometric spectral type of each star is first estimated from its $G - G_{\text{RP}}$ color. The $G - G_{\text{RP}}$ versus spectral type relation for stars with spectral types B0 to L0 is shown in Figure 12. These data were drawn from the list of nearby young association members of Gagné et al. (2018c) and the List of Ultracool Dwarfs,¹⁹ which includes data from previous lists of brown dwarfs (Dupuy & Liu 2012; Mace 2014; Gagné et al. 2015; Faherty et al. 2016; Liu et al. 2016). A polynomial relation was fitted to the data and is also displayed in the figure;

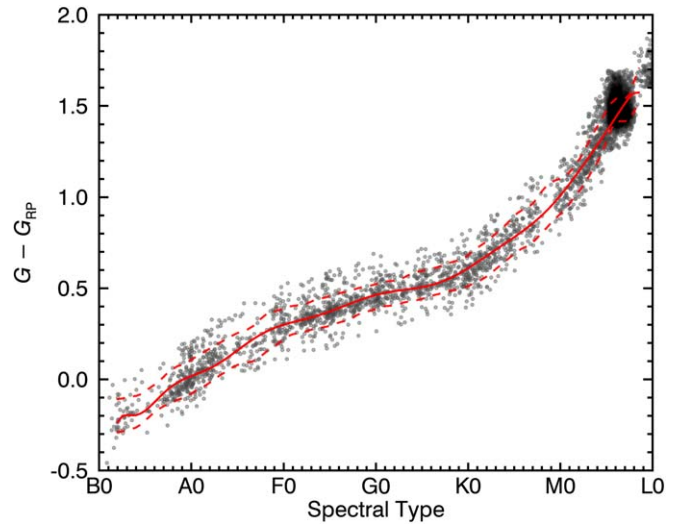


Figure 12. Gaia DR2 $G - G_{\text{RP}}$ colors as a function of spectral type for known nearby young stars and brown dwarfs (black dots). A polynomial fit is shown as a solid red line, with 1σ scatter as a dashed red line. We used this relation to estimate spectral types when no literature data were available. See Section 6.1 for more details. The polynomial coefficients for the red line are available as online-only material.

(The data used to create this figure are available.)

the coefficients to this polynomial sequence are available as online-only material. We preferred using a Gaia DR2 color-to-spectral-type relation rather than a Gaia DR2 absolute-magnitude-to-spectral-type relation, because unresolved multiples would bias the latter more significantly.

We used the Pickles Atlas of spectral energy distributions for B0–M9 stars (Pickles 1998) and interpolated the Gaia DR2 instrumental bandpasses and the extinction curve of Fitzpatrick (1999; with a nominal total to selective extinction value $R(V) = 3.1$) on the Pickles wavelength vector to determine an appropriate extinction correction.

The resulting extinction-corrected $G - G_{\text{RP}}$ color was then used to obtain a better photometric spectral type estimate, which we used in turn to correct the raw $G - G_{\text{RP}}$ color anew. This step was repeated until the photometric spectral type estimate of a star remained unchanged. A total of four iterations were needed for the dereddening correction to converge for all MUTA stars. The resulting extinction vectors and corrected color–magnitude diagram of MUTA are shown in Figure 13.

In Tables 7 and 8, we provide reddening values $R(G)$, $R(G_{\text{RP}})$, and $R(G_{\text{BP}})$ as a function of spectral types or uncorrected Gaia DR2 $G - G_{\text{RP}}$ colors, which can be used to deredden the Gaia DR2 photometry of main-sequence or young stars with the following relations:

$$G_{\text{corr}} = G_{\text{uncorr}} - E(B - V) \cdot R(G), \quad (4)$$

$$G_{\text{RP,corr}} = G_{\text{RP,uncorr}} - E(B - V) \cdot R(G_{\text{RP}}). \quad (5)$$

6. Discussion

In this section, we discuss various properties of the MUTA members and of their population as a whole. Photometric spectral type estimates and additional substellar candidates are discussed in Sections 6.1 and 6.2. This is followed by an estimation of the isochronal age of MUTA (Section 6.3) and a

¹⁹ Available at http://astro.umontreal.ca/~gagne/ultracool_dwarfs.php.

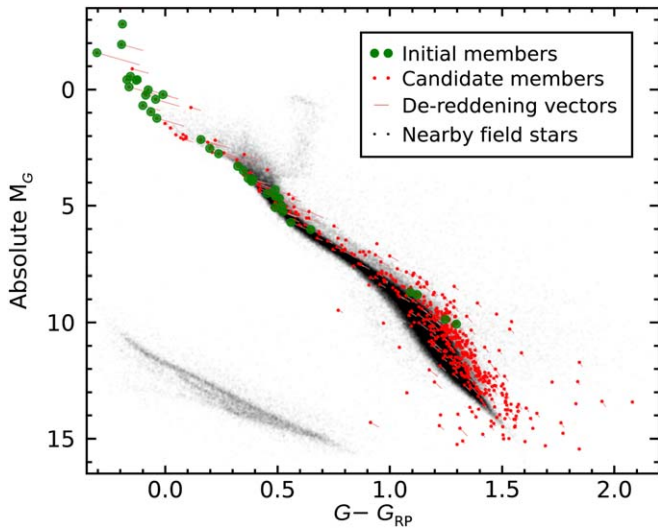


Figure 13. Gaia DR2 color–magnitude diagram of our initial list of MUTA members (green circles) and additional candidate members (red dots). Dereddening vectors are indicated with red lines (dots are located at the corrected position). A proper dereddening correction that accounts for the wide Gaia DR2 bandpasses moves low-mass stars parallel to the sequence and moves higher-mass stars mostly toward the left. See Section 5 for more details.

Table 7

Gaia DR2 Dereddening Relations as a Function of Spectral Type That Account for Its Large Photometric Bandpasses

Spectral Type	$R(G)$ (mag)	$R(G_{RP})$ (mag)	$R(G_{BP})$ (mag)
B3	3.112 ± 0.001	1.938 ± 0.001	3.670 ± 0.001
B5	3.10 ± 0.02	1.936 ± 0.002	3.65 ± 0.02
B7	3.029 ± 0.001	1.926 ± 0.001	3.566 ± 0.001
B9	3.002 ± 0.006	1.925 ± 0.001	3.540 ± 0.006
A1	2.962 ± 0.003	1.919 ± 0.001	3.503 ± 0.002
A3	2.939 ± 0.006	1.916 ± 0.001	3.488 ± 0.004
A5	2.880 ± 0.001	1.904 ± 0.001	3.452 ± 0.001
A7	2.840 ± 0.001	1.901 ± 0.001	3.431 ± 0.001
A9	2.782 ± 0.001	1.893 ± 0.001	3.400 ± 0.001
F1	2.724 ± 0.001	1.885 ± 0.001	3.369 ± 0.001
F3	2.724 ± 0.001	1.885 ± 0.001	3.369 ± 0.001
F5	2.693 ± 0.005	1.883 ± 0.001	3.348 ± 0.002
F7	2.637 ± 0.001	1.874 ± 0.001	3.311 ± 0.001
F9	2.632 ± 0.003	1.873 ± 0.001	3.308 ± 0.002
G1	2.61 ± 0.01	1.869 ± 0.001	3.291 ± 0.009
G3	2.577 ± 0.004	1.865 ± 0.001	3.264 ± 0.004
G5	2.568 ± 0.001	1.864 ± 0.001	3.254 ± 0.001
G7	2.55 ± 0.01	1.864 ± 0.001	3.240 ± 0.008
G9	2.526 ± 0.004	1.863 ± 0.001	3.221 ± 0.003
K1	2.491 ± 0.008	1.858 ± 0.001	3.192 ± 0.008
K3	2.40 ± 0.01	1.843 ± 0.002	3.128 ± 0.007
K5	2.316 ± 0.008	1.829 ± 0.001	3.052 ± 0.008
K7	2.224 ± 0.001	1.803 ± 0.001	2.997 ± 0.001
K9	2.193 ± 0.004	1.786 ± 0.002	3.004 ± 0.001
M1	2.118 ± 0.006	1.755 ± 0.002	2.985 ± 0.003
M3	1.960 ± 0.006	1.699 ± 0.002	2.949 ± 0.001
M5	1.847 ± 0.003	1.654 ± 0.001	2.922 ± 0.001

Note. See Section 5 for more details.

discussion of the cooling ages of the two hot white dwarf candidate members of MUTA (Section 6.4). We discuss literature lithium absorption measurements for K- to G-type members of MUTA in Section 6.5, and we discuss the present-

Table 8

Gaia DR2 Dereddening Relations as a Function of Uncorrected $G - G_{RP}$

Uncorrected $G - G_{RP}$	$R(G)$ (mag)	$R(G_{RP})$ (mag)	$R(G_{BP})$ (mag)
-0.18	1.938 ± 0.001	3.112 ± 0.001	3.670 ± 0.001
-0.08	1.930 ± 0.002	3.05 ± 0.02	3.59 ± 0.02
0.02	1.923 ± 0.002	2.99 ± 0.01	3.53 ± 0.01
0.12	1.919 ± 0.001	2.961 ± 0.009	3.504 ± 0.007
0.22	1.908 ± 0.003	2.90 ± 0.02	3.47 ± 0.01
0.32	1.90 ± 0.01	2.80 ± 0.08	3.40 ± 0.05
0.42	1.881 ± 0.003	2.68 ± 0.03	3.34 ± 0.02
0.52	1.865 ± 0.001	2.570 ± 0.005	3.257 ± 0.004
0.62	1.860 ± 0.001	2.507 ± 0.006	3.206 ± 0.006
0.72	1.842 ± 0.001	2.397 ± 0.009	3.124 ± 0.007
0.82	1.823 ± 0.005	2.30 ± 0.02	3.04 ± 0.01
0.92	1.796 ± 0.003	2.211 ± 0.005	3.000 ± 0.001
1.02	1.769 ± 0.003	2.157 ± 0.006	3.000 ± 0.001
1.12	1.735 ± 0.003	2.057 ± 0.008	2.965 ± 0.001
1.22	1.687 ± 0.002	1.930 ± 0.004	2.944 ± 0.001
1.32	1.656 ± 0.001	1.852 ± 0.003	2.924 ± 0.001
1.42	1.641 ± 0.001	1.818 ± 0.001	2.912 ± 0.001

Note. See Section 5 for more details.

day mass function of MUTA in Section 6.6. The stellar activity of its members is assessed in Section 6.7. MUTA is placed in context with the Galactic kinematic structure recently unveiled by Kounkel & Covey (2019) in Section 6.8.

6.1. Photometric Spectral Type Estimates

The extinction correction method described above directly provides photometric spectral type estimates for MUTA candidates and members with no spectral type information in the literature. We used a slightly different method to estimate the photometric spectral types of objects near the substellar regime with near-infrared 2MASS–WISE colors $J - W2 > 1.5$, corresponding to spectral types $\simeq M6$ and later (Gagné et al. 2015). For these redder objects, we used the spectral type to $J - W2$ relation of Gagné et al. (2015) to determine a more accurate subtype given that the Gaia DR2 $G - G_{RP}$ colors are more spread and based on lower-quality detections in these cases (see, e.g., Smart et al. 2019). All photometric spectral type estimates are shown in Figure 14.

6.2. Substellar Objects

In Figures 15 and 16, we show near-infrared color–magnitude sequences of MUTA candidates based on 2MASS and WISE photometry, compared with those of field-aged and young L-type or later low-mass stars and brown dwarfs. In both cases, the MUTA sequence forms a prolongation of the young substellar sequences at brighter absolute magnitudes, and there is a small overlap indicating that a few MUTA candidates discussed here may have spectral types as late as $\simeq L0$ (although at the age of MUTA the substellar boundary is near spectral type M7; Allard et al. 2012; Baraffe et al. 2015; Filippazzo et al. 2015). Kirkpatrick et al. (2011) devised a rejection criterion based on WISE photometry to distinguish extragalactic sources from brown dwarfs, but our only MUTA candidates with a sufficient W3-band detection were not red enough in $W1 - W2$ color to apply the rejection criterion.

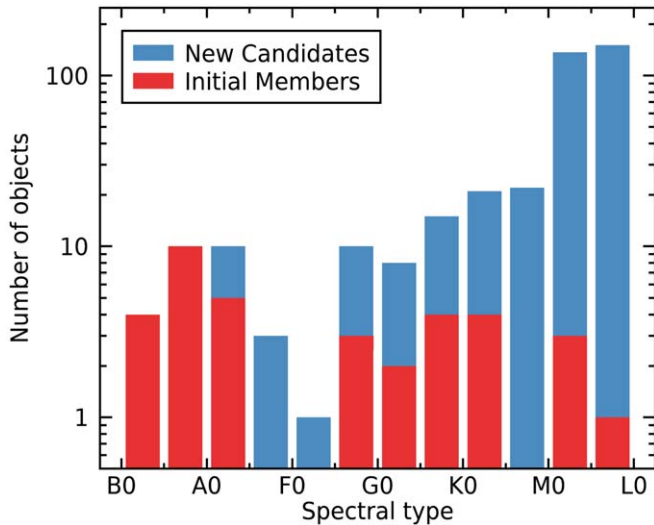


Figure 14. Distribution of observed and estimated photometric spectral types for initial MUTA members (red bars) and candidate members (blue bars). Data from Gaia DR2 allowed us to recover candidate members with photometric spectral types as late as M9. Two hot white dwarf candidates are excluded from this figure. See Section 6.1 for more details.

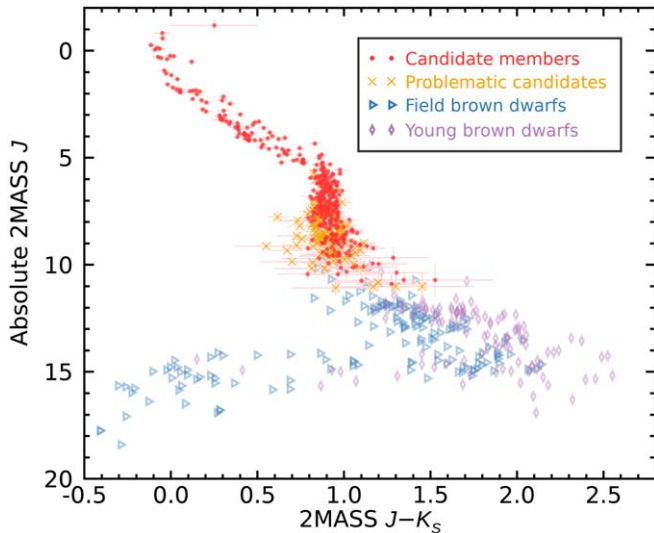


Figure 15. Absolute 2MASS J -band magnitudes vs. $J - K_s$ colors for field (rightward-pointing blue triangles) and young (purple diamonds) brown dwarfs compared with all MUTA candidates and members (filled red circles). The MUTA candidates barely reach the sequence of young L-type brown dwarfs and seem brighter or redder than the field brown dwarf sequence, as expected for young objects. A fraction of the candidates with problematic Gaia DR2 colors (orange crosses) do not follow the MUTA sequence, which is expected if their photometry is contaminated by background objects. Only spectral types L0 and later are shown for all brown dwarf data. See Section 6.2 for more details.

6.3. Isochronal Age

The locus of MUTA candidates and members compiled in this work forms a sequence in color–magnitude space that sits between those of the Pleiades association (112 ± 5 Myr; Dahm 2015) and the Tucana-Horologium (see Torres et al. 2000; Zuckerman et al. 2001b), Columba and Carina associations ($\simeq 45$ Myr; Torres et al. 2008; Bell et al. 2015). We cross-matched all bona fide members of these four associations compiled by Gagné et al. (2018c) with Gaia DR2 for this

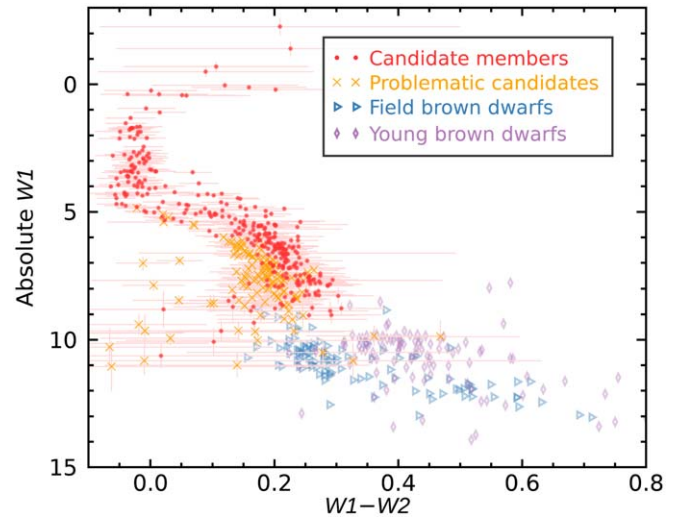


Figure 16. Absolute WISE W1-band magnitudes vs. $W1 - W2$ colors for field and young brown dwarfs compared with all MUTA candidates and members. Color coding is the same as for Figure 15. Only spectral types L0 and later are shown for brown dwarf data. See Section 6.2 for more details.

comparison and built an empirical isochrone for each of them by fitting their sequence with a high-order polynomial. The cross-matches with Gaia DR2 were all inspected for spurious matches by building finder charts similar to those discussed in Section 4.5. The color–magnitude positions of all members were corrected for extinction by interstellar dust with the method described in Section 5. This procedure only had a noticeable but small effect on the Pleiades members.

All known unresolved binaries were removed from these lists, and their color–magnitude diagrams were visually inspected to remove the obvious sequence of unresolved binaries and triples that were shifted up by 0.75 and 1.19 mag in Gaia DR2 G -band magnitude, respectively. The detailed lists of members used to build these isochrones will be presented in an upcoming publication, along with those of other nearby young associations.

Representing a young association’s color–magnitude sequence with a polynomial curve can be complicated by the fact that they contain many more low-mass stars (e.g., Bochanski et al. 2010), which would cause an overfitting of the data in the red part of the color–magnitude diagram. To avoid this, we first build a moving box average and standard deviation of the members’ absolute Gaia DR2 G -band magnitudes in bins of 0.05 mag in $G - G_{RP}$ colors, and we subsequently fit an 11-order (Tucana-Horologium, Columba, and Carina) or 15-order (Pleiades) polynomial, which were found to be appropriate given the number of stars and the range of colors occupied by the members of these associations. Columba, Tucana-Horologium, and Carina were combined as a single $\simeq 45$ Myr old population, as they all share the same age (Bell et al. 2015). This allowed us to build a more accurate empirical isochrone given the larger number of resulting members.

We used our initial list of MUTA members (Table 1) to determine an isochronal age for the association, by comparing each member’s absolute G -band magnitude with a hybrid isochrone built from a weighted sum of the $\simeq 45$ and $\simeq 112$ Myr empirical isochrones described above. We assumed that the members are spread around the best-fitting hybrid isochrone along a Gaussian likelihood with a standard deviation of

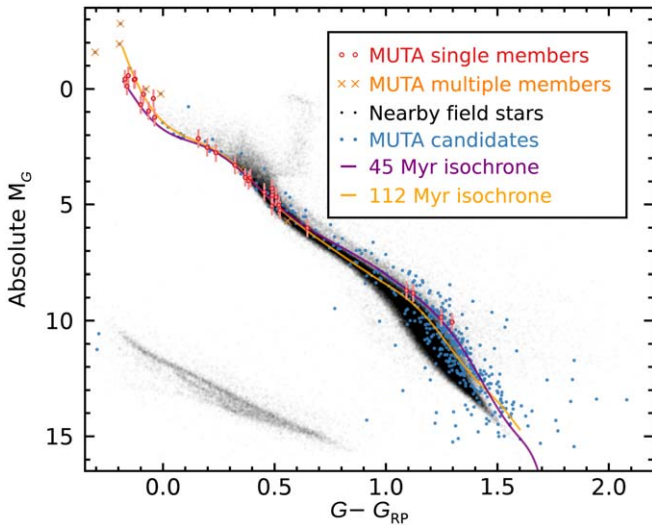


Figure 17. Gaia DR2 color–magnitude diagram of MUTA members used for isochrone fitting (red filled circles) and other candidates (blue filled circles) compared with field stars within 100 pc of the Sun (black dots) and empirical isochrones built from the Pleiades associations (orange line) and a combination of the Tucana-Horologium, Carina, and Columba associations (purple line). MUTA objects flagged as potential unresolved or contaminated objects are identified with orange crosses. See Section 6.3 for more details.

0.35 mag, typical of other young associations. Members that either are known binaries or have a Gaia DR2 RUWE above 1.4 were not used for this isochronal age determination. The latter objects are identified in Figure 17, along with the empirical isochrones built from the Pleiades and the Tucana-Horologium, Columba, and Carina associations.

A one-dimensional grid search was performed to identify the linear combination of the $\simeq 45$ and $\simeq 112$ Myr empirical isochrones that best matches the MUTA stars. A thousand values for a linear coefficient α_i were chosen with $\alpha \in [0, 1]$ to build a set of hybrid isochrones I_i built from the $\simeq 45$ Myr isochrone I_{45} and the $\simeq 112$ Myr isochrone I_{112} :

$$I_i = \alpha_i \cdot I_{45} + (1 - \alpha_i) \cdot I_{112}. \quad (6)$$

The goodness of fit of each hybrid isochrone for the 10^3 values of α_i was assessed by calculating the Gaussian likelihood that the Gaia DR2 absolute G -band magnitudes of MUTA members y_j and their associated standard deviations σ_j match the model I_{ij} in each color bin j :

$$\ln P_i = -0.5 \cdot \sum_j \left(\frac{y_j - I_{ij}}{\sigma_j + 0.35 \text{ mag}} \right)^2. \quad (7)$$

The best-fitting linear combination is displayed in Figure 18. The ages A_i corresponding to each hybrid isochrone I_i were taken as a linear combination of the individual empirical isochrones in logarithm space:

$$\log A_i = \alpha_i \cdot \log(45 \text{ Myr}) + (1 - \alpha_i) \cdot \log(112 \text{ Myr}). \quad (8)$$

The resulting probability density function $P(A_i)$ is shown in Figure 19. It is well represented by a Gaussian in logarithm of age, with an average and characteristic width that correspond to $\log A(\text{yr}) = 7.79 \pm 0.05$, or an age of 62 ± 7 Myr.

We also calculated a probability density function for the relative age parameter α because the age estimates of both our reference populations could change in the future. For example, some recent lithium depletion boundary age estimates for the Pleiades are as old as 148 ± 19 Myr (Burke et al. 2004), and

Kraus et al. (2014) estimated a slightly younger age for Tucana-Horologium based on the lithium depletion boundary: they found ages of 38 ± 2 Myr or 41 ± 2 Myr, depending on the evolutionary models that they used. The age of MUTA can thus be refined with the equation above (i.e., a simple interpolation in log age), replacing α_i with a Gaussian probability density function at 0.65 ± 0.12 for α . Using the two extreme ends of these age estimates for the Pleiades and Tucana-Horologium would correspond to MUTA ages of 55 ± 7 Myr, or 69 ± 10 Myr, placing two conservative boundaries for the possible age of MUTA.

All MUTA candidate members located more than 0.35 mag fainter than the best-fitting hybrid isochrone were marked as problematic candidates because they likely correspond to interloping field-aged M dwarfs or contaminated Gaia DR2 entries. This flagging procedure is displayed in Figure 20. This step has removed 135 objects from our list of good-quality candidates; we note that this number is comparable to the number of contaminants (192_{-22}^{+25}) we have estimated in Section 4.3 based on the number of old white dwarf interlopers.

6.4. White Dwarf Cooling Ages

In Section 4.3, we noted that our search for additional MUTA candidates yielded 12 white dwarfs seemingly comoving with MUTA, 10 of which are clearly too cold, and therefore too old, to be credible members. The only two exceptions are WD 0340+103 (MUTA 125) and WD 0350+098 (MUTA 190), which seem to be aged about 200–800 Myr from a first comparison with total-age cooling tracks. However, both white dwarfs are so hot that a direct comparison of color–magnitude relations at visible wavelengths is imprecise, as this regime only samples the Rayleigh–Jeans end of their spectral energy distributions. Furthermore, the Gaia DR2 dereddening procedure developed here cannot be applied to white dwarfs directly. For this reason, we investigated the properties of both white dwarfs in more detail.

WD 0340+103 is an extremely hot white dwarf, whose properties have been estimated at $\log g = 8.6$, $T_{\text{eff}} = 42,617$ K, and a mass of $1.03 M_{\odot}$ by Gentile Fusillo et al. (2019). However, these properties were obtained by fitting models to the Gaia DR2 photometry of WD 0340+103, and the visible photometry of hot stars is relatively insensitive to their fundamental properties given that it only samples the Rayleigh–Jeans limit of their spectral energy distribution. For this reason, we obtained more reliable fundamental parameters by making use of spectroscopy instead of photometry.

We first determined the effective temperature and surface gravity of WD 0340+103 by fitting its SDSS optical spectrum (Ahn et al. 2012) with the grid of non-local thermodynamic equilibrium atmosphere models of Bédard et al. (2020). This yielded a very hot temperature of $83,000 \pm 2000$ K and $\log g = 8.83 \pm 0.08$. Because WD 0340+103 only exhibits hydrogen features given its DA spectral type, we assumed a pure-hydrogen atmospheric composition. We used the fitting procedure described in Bergeron et al. (1992) and Liebert et al. (2005): briefly, the normalized Balmer lines are adjusted with the theoretical line profiles using the Levenberg–Marquardt least-squares method. The observed spectrum of WD 0340+103 was well reproduced by this method, including the emission component at the core of the $H\alpha$ line, as illustrated in Figure 21. The positions of the lower Balmer lines ($H\alpha$, $H\beta$, and $H\gamma$) were used to measure a total redshift of

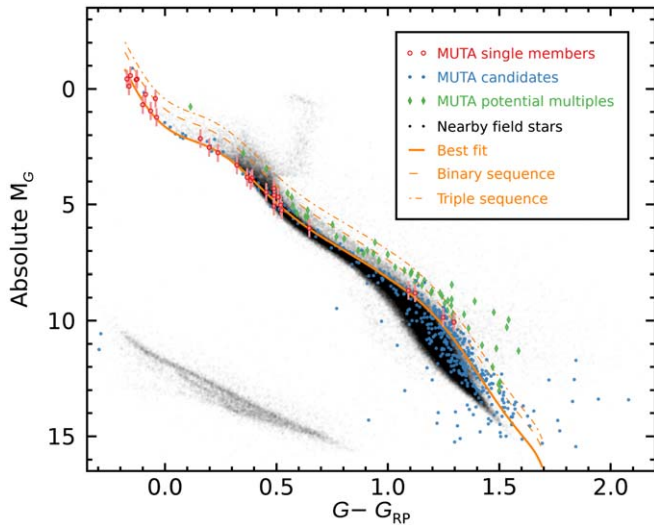


Figure 18. MUTA members used for isochrone fitting (red circles and error bars) fitted with a linear combination of empirical isochrones. The best fit, corresponding to an age of 62 ± 7 Myr, is represented with an orange line. Similar isochrones shifted by 0.75 and 1.19 mag are also shown as orange dashed and dashed-dotted lines, respectively, to represent the locations of unresolved equal-luminosity binaries and triples. Other candidate members of MUTA are shown as blue circles, and those flagged as possible binaries are shown as green diamonds. See Section 6.3 for more details.

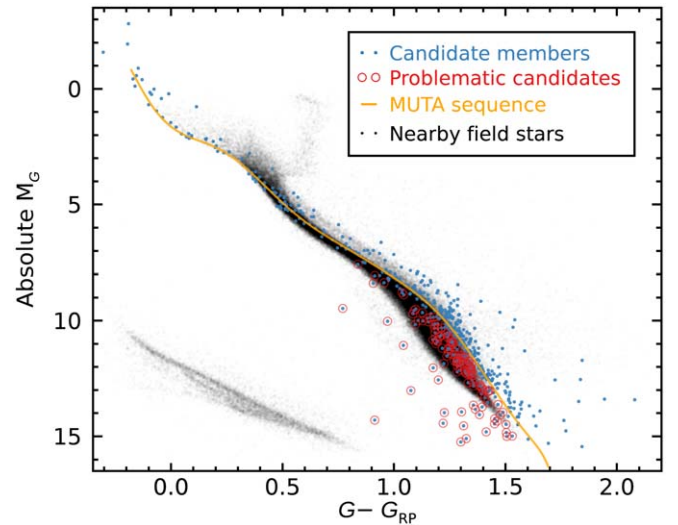


Figure 20. Gaia DR2 color-magnitude diagram of MUTA members and candidates (blue dots) compared with nearby Gaia DR2 entries (black dots) and the best-fitting hybrid isochrone for MUTA members. We identified all candidates with an absolute magnitude more than 0.35 mag fainter than this hybrid isochrone as problematic because they likely correspond to bad Gaia DR2 astrometric solutions, field-aged low-mass stars that have kinematics similar to MUTA by chance, or sources contaminated by a background object. See Section 6.3 for more details.

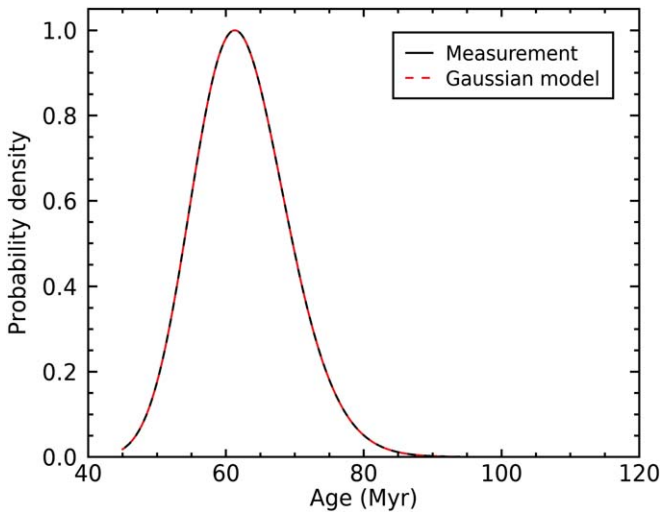


Figure 19. Relative probability density function for the isochronal age of MUTA determined from fitting a combination of empirical isochrones of nearby young associations (black line). A normal probability density function in logarithm age is also shown (red dashed line). The observed MUTA age is well represented by a Gaussian distribution at 62 ± 7 Myr. See Section 6.3 for more details.

$138 \pm 21 \text{ km s}^{-1}$, due in part to the gravitational redshift and radial velocity of WD 0340+103.

In a second step, we calculated the mass, radius, luminosity, and cooling age that correspond to the effective temperature and surface gravity of WD 0340+103 using the thick hydrogen layer ($M_{\text{H}}/M = 10^{-4}$) cooling tracks of Bédard et al. (2020), which are appropriate for the study of hot white dwarfs. Following Holberg & Bergeron (2006), we also computed the absolute SDSS g -band magnitude, which we combined with the observed (dereddened) SDSS g -band magnitude to evaluate

its spectroscopic distance. The atmospheric and stellar parameters of WD 0340+103 are summarized in Table 9. Our analysis shows that WD 0340+103 is a highly unusual white dwarf: it is extremely hot, young, and massive. Furthermore, we note that the spectroscopic distance is slightly farther than its Gaia DR2 trigonometric distance, but the values are consistent within measurement errors.

We used the MESA Isochrones and Stellar Tracks (MIST; Choi et al. 2016) to estimate a progenitor mass of $6.7 \pm 0.4 M_{\odot}$ for WD 0340+103. This corresponds to a spectral type of about B2, just one subclass earlier than the earliest-type members of MUTA (29 Tau, 30 Tau, μ Tau, and μ Eri are all B3 stars). This is consistent with the extremely young cooling age of only $270,000 \pm 30,000$ yr that we derived for WD 0340+103. Such a progenitor star has a main-sequence lifetime of 59_{-6}^{+8} Myr, corresponding to a total age of 60_{-6}^{+8} Myr, consistent with our isochronal age of 62 ± 7 Myr. Combining both estimates in an error-weighted average allows us to refine our age estimate for MUTA at 61 ± 5 Myr. The core composition of this massive white dwarf likely does not consist of carbon and oxygen, but rather oxygen and neon (Lauffer et al. 2018; Camisassa et al. 2019). This is expected to have a significant effect on the calculated cooling age of about 20% (see, e.g., Simon et al. 2015; Gagné et al. 2018b; Simon 2018), however, in the present scenario the age estimate of WD 0340+103 is completely dominated by its main-sequence lifetime, and its core composition will therefore not have any significant effect on our total-age estimation.

The detailed properties of WD 0350+098 are harder to determine because of its lack of spectral lines, likely due to extreme Zeeman broadening caused by a strong magnetic field. Much like WD 0340+103, the age estimate based on Gaia DR2 photometry alone may be unreliable given its extremely blue colors and hot temperature. Adding UV photometry from GALEX (Martin et al. 2005) to better constrain its temperature yielded an estimate of

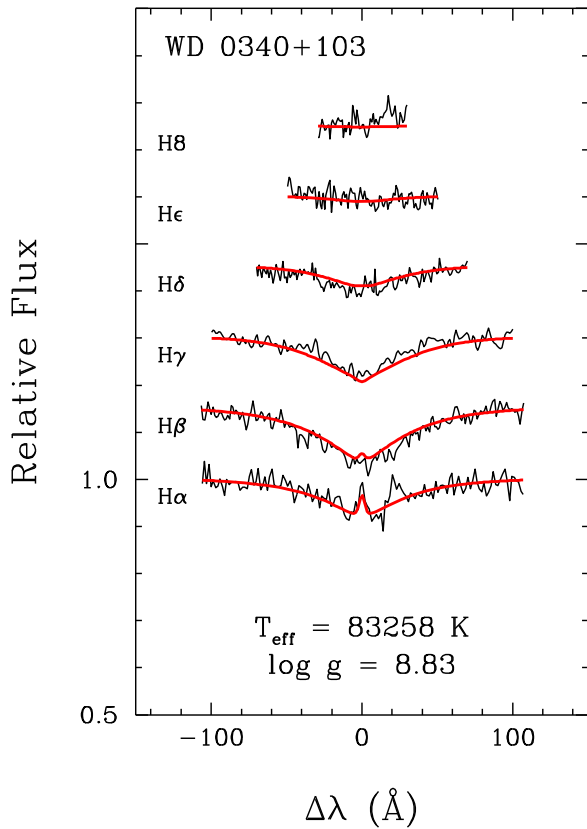


Figure 21. Model fit to the Balmer lines of WD 0340+103 (MUTA 125). See Section 6.4 for more details.

$31,000 \pm 1000$ K with a radius of $0.0073^{+0.0006}_{-0.0005} R_{\odot}$; however, these uncertainties are likely underestimated because the models we used do not include magnetic fields. These parameters would correspond to a mass of $1.09^{+0.04}_{-0.05} M_{\odot}$ and a surface gravity of $\log g = 8.75 \pm 0.09$. Using nonmagnetic cooling tracks yields a cooling age estimate of 79^{+20}_{-10} Myr. The main-sequence lifetime that corresponds to the $6.1 \pm 0.5 M_{\odot}$ progenitor is 74^{+15}_{-12} Myr, making WD 0350+098 too old for MUTA membership if we take our analysis at face value. However, the lack of magnetic fields in our treatment could have introduced a significant bias in the determination of its cooling age and mass (and therefore its main-sequence lifetime), and for this reason we keep it as a candidate member of MUTA.

6.5. Lithium

The equivalent width of the Li I $\lambda 6708$ spectral line is a well-established age indicator. Because lithium burns at lower temperatures than hydrogen, it is relatively fragile and will disappear over time if it is allowed to be transported to layers deep enough in a star to reach the threshold temperature for lithium burning. The temperature profile of a star, combined with the location of its convective layers, will determine whether lithium gets burned at all and how fast it does so. Low-mass stars (late K or early M spectral types) have deep convective layers that allow them to burn through all lithium within only $\simeq 30$ Myr (Randich 2001), whereas higher-mass stars, with their shallower convective layers, burn lithium more gradually. It takes more than a billion years for stars with spectral types G0 and earlier to burn lithium in their

Table 9
Properties of WD 0340+103 (MUTA 125)

Property	Value	References
Position and Kinematics		
Gaia DR2 Source ID	36321786805002880	1
R.A. ep. 2015.5 ^a	03:43:14.370 \pm 0.09	1
Decl. ep. 2015.5 ^a	+10:29:38.15 \pm 0.06	1
$\mu_{\alpha} \cos \delta$ (mas yr ⁻¹)	31.51 \pm 0.18	1
μ_{δ} (mas yr ⁻¹)	-22.55 \pm 0.12	1
Parallax (mas)	6.8 \pm 0.1	1
Trigonometric distance (pc)	145.7 \pm 2.3	1
Spectroscopic distance (pc)	163.4 ⁺¹⁶ ₋₁₅	2
RV _{opt} ^b (km s ⁻¹)	14.3 \pm 3.4	2
RV _{mes} (km s ⁻¹)	27 \pm 21	2
Photometric Properties		
G_{BP} (Gaia DR2)	16.307 \pm 0.009	1
G (Gaia DR2)	16.539 \pm 0.001	1
G_{RP} (Gaia DR2)	16.766 \pm 0.005	1
u_{AB} (SDSS DR12)	15.946 \pm 0.005	3
g_{AB} (SDSS DR12)	16.298 \pm 0.003	3
r_{AB} (SDSS DR12)	16.748 \pm 0.004	3
i_{AB} (SDSS DR12)	17.090 \pm 0.005	3
z_{AB} (SDSS DR12)	17.392 \pm 0.016	3
Fundamental Properties		
Spectral type	DA	4
T_{eff} (K)	83,000 \pm 2000	2
$\log g$	8.83 \pm 0.08	2
Mass (M_{\odot})	1.16 \pm 0.04	2
Radius (R_{\odot})	0.0069 ^{+0.0006} _{-0.0005}	2
$\log L/L_{\odot}$	0.31 \pm 0.08	2
Cooling age (Myr)	0.27 \pm 0.03	2
Progenitor mass (M_{\odot})	6.7 \pm 0.4	2
Progenitor spectral type	B2	2
Total age (Myr)	60 ⁺⁸ ₋₆	2

Notes.

^a J2000 position at epoch 2015.5 from the Gaia DR2 catalog. Measurement errors are given in units of milliarcseconds.

^b Optimal radial velocity predicted by BANYAN Σ that assumes membership in MUTA.

References. (1) Gaia Collaboration et al. 2018; (2) this work; (3) Alam et al. 2015; (4) Kleinman et al. 2013.

photospheres such that the Li I $\lambda 6708$ absorption line disappears completely (Jones et al. 1999). As a result, the sequence in temperature versus Li I absorption line for K-type or earlier stars evolves slowly with time and makes it possible to place weak constraints on the age of a coeval population of such early-type stars (e.g., Barrado y Navascués et al. 2001; Soderblom et al. 1993). Similarly, the K-type lithium depletion boundary, where stars below a given temperature stop displaying the lithium absorption line, can be used to place constraints on the age of a stellar population. The location of this boundary is, however, not very sensitive to age for populations $\simeq 10$ Myr and older (Kraus et al. 2014).

Brown dwarfs with masses below $\simeq 60 M_{\text{Jup}}$ do not burn lithium despite their fully convective structure, because they do not reach temperatures sufficient to do so even at their core (e.g., Baraffe et al. 2015). Low-mass stars and brown dwarfs with masses above $60 M_{\text{Jup}}$ burn their photosphere lithium slowly, causing the appearance of a second, age-dependent boundary where the lithium absorption line begins appearing again below a threshold in effective temperature. The effective temperatures, spectral types, and bolometric luminosities at

Table 10
Lithium Equivalent Width Measurements for MUTA

MUTA ID	Common Name	ROSAT Name	EW(Li) (mÅ)	T_{eff} (K)	T_{eff} References
24	RX J0348.5+0832	RX J0348.5+0832	260	5409	2
27	RX J0338.3+1020	RX J0338.3+1020	250	5250	2
29	RX J0358.2+0932	RX J0358.1+0932	200	4855	1
94	V1267 Tau	RX J0333.1+1036	320	4967	1
159	TYC 71–542–1	RX J0347.9+0616	200	5794	2
195	2MASS J03545074+1232061	RX J0354.8+1232	0	4028	3
318 A	2MASS J04341953+0226260	RX J0434.3+0226	300	4714	1
350	TYC 91–702–1	RX J0442.9+0400	220	5247	2
362	V1831 Ori	RX J0450.0+0151	350	5247	1
376	TYC 665–150–1	RX J0357.3+1258	250	5943	2

Notes. All lithium equivalent width measurements are from Magazzù et al. (1997). TYC 665–150–1 was excluded from Figure 22 because it is a low-likelihood candidate member of MUTA (its separation from the MUTA model in UVW space is 8.1 km s^{-1}). See Section 6.5 for more details.

References. (1) Bai et al. 2019; (2) Xing 2010; (3) Gaia Collaboration et al. 2018.

(This table is available in machine-readable form.)

which this second, M-type lithium depletion boundary occurs are a strong function of age over the first hundreds of millions of years that follow stellar formation. The lithium depletion boundary has therefore become a popular diagnostic tool to determine precise ages for stellar populations with known M-type stars (e.g., Kraus et al. 2014; Malo et al. 2014b; Shkolnik et al. 2017).

Measuring the equivalent width of the lithium absorption line accurately requires high-resolution spectroscopy, ideally with a resolving power $\lambda/\Delta\lambda > 10,000$ to avoid contamination from otherwise blended spectral lines such as Fe I (Xing 2010). Such measurements require long exposure times, and they have thus typically only been obtained for known populations of nearby associations or open clusters. However, a literature search revealed that Li I equivalent width measurements have been obtained by Magazzù et al. (1997) for nine members or candidate members (and one low-likelihood candidate) of MUTA in a follow-up of ROSAT X-ray-bright sources (Neuhäuser et al. 1995) in the vicinity of Taurus-Auriga. These measurements were obtained at a relatively low resolving power ($\lambda/\Delta\lambda \simeq 8400$),²⁰ meaning that the equivalent widths may be slightly overestimated because of line blending. We obtained effective temperatures for these 10 stars from Xing (2010), Gaia Collaboration et al. (2018), and Bai et al. (2019), where available, and listed them in Table 10 along with the lithium equivalent width measurements of Magazzù et al. (1997).

In Figure 22, we compare these available MUTA temperature versus lithium measurements with other literature data for stellar populations across a range of ages. The 20–25 Myr sequence was built from the β Pictoris moving group (β PMG; see, e.g., Zuckerman et al. 2001a; Zuckerman & Song 2004; Bell et al. 2015; measurements are from Mentuch et al. 2008; Malo et al. 2014b; Shkolnik et al. 2017). The 40–50 Myr sequence was built from the stellar populations of the Tucana-Horologium association discussed earlier (lithium equivalent width measurements are by Kraus et al. 2014) and the IC 2602 and IC 2391 open clusters (Randich 2001; Barrado y

Navascués et al. 2004; Dobbie et al. 2010). The 110–125 Myr sequence was built from the Pleiades association (Soderblom et al. 1993; Jones et al. 1996; Bouvier et al. 2018), and the 150–175 Myr sequence was built from the M35 open cluster (Barrado y Navascués et al. 2001; Bouy et al. 2015).

Although the available MUTA measurements do not span either of the lithium depletion boundaries, they seem consistent with an age in the range of 20–125 Myr, with the caveat that our comparison sequences were built from higher-resolution spectra compared with MUTA measurements. This likely biases our range slightly toward young ages, but this result seems consistent with our previous age assessments based on empirical isochrones and white dwarf cooling ages. Obtaining higher-resolution optical spectra for MUTA members, as well as extending the range of spectral types over which lithium equivalent widths are measured, will allow us to further constrain the age of MUTA.

6.6. Present-day Mass Function

We used the empirically corrected MIST solar-metallicity model isochrones of Choi et al. (2016) as described by Gagné et al. (2018a),²¹ with a nominal stellar rotation of $v/v_{\text{crit}} = 0$ to estimate the masses of MUTA members and candidates based on their position in a Gaia DR2 absolute G versus $G - G_{\text{RP}}$ color-magnitude diagram. This method uses the differences between the empirical Pleiades sequence and the 112 Myr MIST isochrone to correct for systematic effects such as the increased stellar activity and strong magnetic fields of low-mass stars.

The masses for MUTA candidates with very red colors ($J - W2 > 1.5$) were estimated with the method of Gagné et al. (2014), which is more reliable than extrapolating MIST isochrones or using lower-quality Gaia DR2 photometry but potentially suffers from different systematics. The method is based on a comparison of the absolute 2MASS J , H , K_S and WISE W1 and W2 photometry of MUTA candidates with BT-Settl models (Allard et al. 2012) in the same respective bandpasses and combining the individual estimates in a likelihood analysis. These model-dependent mass estimates

²⁰ Magazzù et al. (1997) also obtained measurements at $\lambda/\Delta\lambda \simeq 4200$, but inspecting the Isaac Newton Group Archive at <http://casu.ast.cam.ac.uk/casuadc/ingarch/query> indicated that none of these lower-resolution observations have been obtained for MUTA objects.

²¹ We used the models based on the revised Gaia DR2 photometric zero-points of Evans et al. (2018a) available at http://waps.cfa.harvard.edu/MIST/model_grids.html.

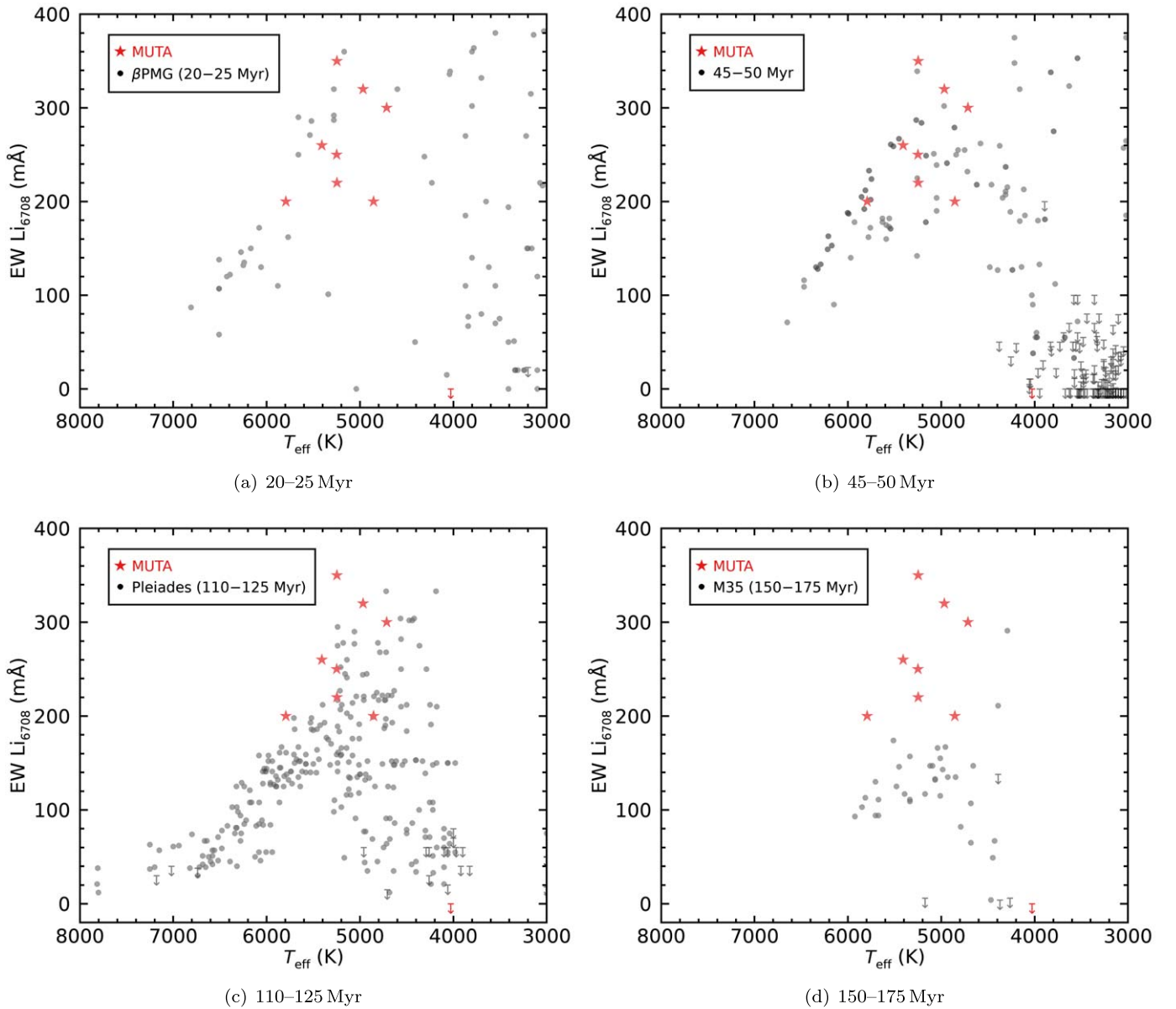


Figure 22. Effective temperature vs. the equivalent width of the Li I $\lambda 6708$ absorption line for MUTA members and candidates (red stars), compared with other known, coeval populations (gray circles). The 45–50 Myr sequence was built from members of the Tucana-Horologium association and IC 2602 and IC 2391 open clusters. Upper limits are indicated with downward-pointing arrows. Although all measurements for MUTA members are based on a lower resolving power ($\lambda/\Delta\lambda \approx 8400$) compared with the reference sequences ($\lambda/\Delta\lambda > 10,000$), they indicate that MUTA seems roughly consistent with an age of 20–125 Myr. β PMG indicates the β Pictoris moving group. See Section 6.5 for more details.

range from $\approx 35 M_{\text{Jup}}$ to $0.2 M_{\odot}$, covering the substellar-to-stellar transition and overlapping slightly with the range of masses (0.1 – $6.0 M_{\odot}$) obtained with MIST isochrones for bluer targets.

The resulting present-day mass function of MUTA members and candidates is displayed in Figure 23, along with a fiducial log-normal mass function ($\sigma = 0.5$ dex, $m_c = 0.25 M_{\odot}$). We fitted its amplitude to our MUTA members with masses above $1 M_{\odot}$, but the width and central position were not fitted. This particular mass function was shown to be a good fit to other nearby young associations by Jeffries (2012). The lognormal mass function is a good match to our distribution of MUTA members and candidates down to $0.1 M_{\odot}$, indicating that its present-day mass function may be similar to other young associations of the solar neighborhood. Assuming that the population of MUTA is complete above $0.2 M_{\odot}$ indicates that

about 65 brown dwarf members would remain to be found, for a total stellar and substellar population of ≈ 450 members.

6.7. Stellar Rotation and Activity

Young stars lose angular momentum as they age, and their rotation periods consequently slow down with time. Because the rate of angular momentum loss depends on the rotation period, members of stellar associations with a wide range of rotation periods will eventually converge to a tight sequence as a function of their mass (Barnes 2003; van Saders et al. 2016). The timescale for this convergence for Sun-like stars is < 650 Myr and decreases with increasing stellar mass (Delorme et al. 2011; Douglas et al. 2016; Curtis et al. 2019), but a partial sequence is apparent even at ≈ 112 Myr for higher-mass stars (Rebull et al. 2016).

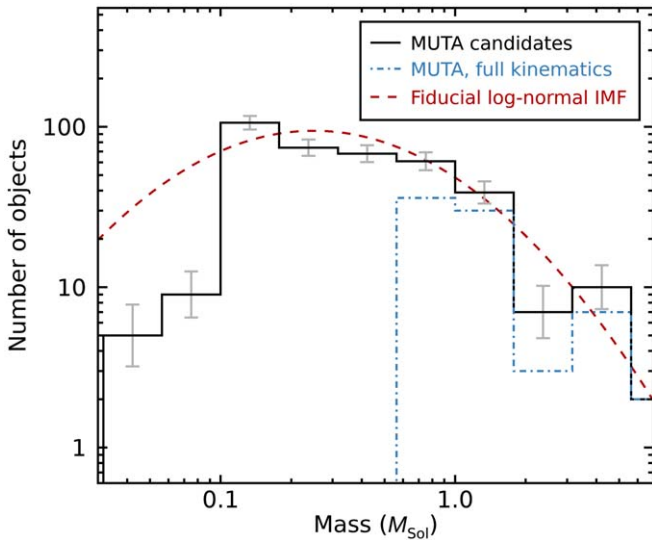


Figure 23. Present-day mass function of MUTA (thick black bars) compared with a fiducial lognormal initial mass function with a peak mass $0.25 M_{\odot}$ and a logarithm characteristic width of 0.5, anchored on the $>0.2 M_{\odot}$ population of MUTA. Gray error bars represent uncertainties associated with Poisson statistics. The subset of members with full kinematics and therefore a more reliable membership are shown with a dashed-dotted blue line. Our set of candidates is consistent with a complete population down to $\approx 0.1 M_{\odot}$ if a lognormal mass function is realistic for MUTA, but the brown dwarf population still seems mostly incomplete. We did not include the progenitor masses of the two white dwarf candidates in this figure. See Section 6.6 for more details.

Depending on the mass, this trend of longer rotation periods for older ages *reverses* for the youngest (pre-main-sequence) stars, as they spin up while contracting onto the main sequence. The youngest stars therefore also have longer rotation periods. The scatter at these younger ages is also larger because of a large spread in the initial rotation periods. Thus, the rotation period versus color sequence of MUTA can still be used as an additional test of our assigned age by comparing with similarly aged groups.

As boundaries on the expected age of MUTA, we used members of the Pleiades (≈ 112 Myr; Dahm 2015) and Praesepe clusters (≈ 800 Myr; Brandt & Huang 2015), in addition to members of the Columba, Carina, and Tucana-Horologium associations discussed earlier (≈ 45 Myr). We included the older Praesepe cluster as an example of a clearly older population in the color–rotation period diagram, because the differences between MUTA and the Pleiades are subtle. We collected the rotation period measurements of the Pleiades and Praesepe members from Rebull et al. (2016) and Douglas et al. (2017), respectively. We obtained light curves for each member of the younger three associations from the TESS or K2 missions, where available. We restricted our sample to targets with Gaia DR2 $G - G_{\text{RP}} > 0.2$, as the variability period in bluer stars may be impacted by pulsations as much as rotation. For those observed by K2 (16 stars), we used K2SFF processed light curves (Vanderburg & Johnson 2014). For TESS targets with short-cadence data, we used light curves from the Science Processing Operations Center (SPOC; Jenkins et al. 2016), and for others we extracted light curves from the full-frame images using Eleanor²² (Feinstein et al. 2019). We excluded targets with flux contamination ratios above 1, even when rotation consistent with youth was present in the curve.

We estimated the rotation periods for each star using two methods: a modified version of the Lomb–Scargle periodogram as described in Horne & Baliunas (1986), and the autocorrelation function as described in McQuillan et al. (2013). In both cases, we searched for periodic signals down to twice the Nyquist-sampling limit, and as long as a third of the total data coverage. Below the lower limit, we found that both algorithms are biased by the data sampling, particularly for long-cadence (30 minutes) data. We set the lower limit for a significant detection at three full rotations. We then flagged the peak in the periodogram and the second peak in the autocorrelation function as the likely period (see Figure 24 for an example). We only considered periodic signals with false-alarm probabilities $< 1\%$ and for which autocorrelation and Lomb–Scargle periods agreed within 10%. For six stars, the autocorrelation and Lomb–Scargle disagreed by an integer factor (alias), which we retained, provided that the true rotation period was clear. Across all clusters, 14 out of 201 stars showed evidence of a second period, which we excluded from our sample, as they are likely binaries (Douglas et al. 2017). As a final check, we visually inspected all phased light curves.

We created synthetic data sets, with random subsamples of half the data and each point perturbed by a random number following the measurement errors, to investigate the accuracy of our period determinations. We found that, when the correct period is identified, our assigned periods are accurate within 2%, with a fail rate of $\approx 5\%$ where the measured period is wrong by 20% or more (usually off by an integer multiple). This assumes that all detected periods are associated with stellar rotation and not other phenomena. Periodic signals caused by binary systems, pulsations, or flares could cause further false positives, if they passed our visual inspection.

The resulting rotation periods are shown in Figure 25 and listed in Table 11. While there is significant scatter in the sequence, Praesepe and Pleiades members have the longest typical rotation period at $G - G_{\text{RP}} < 0.8$, while members of younger moving groups have the shortest periods, and MUTA members are located in between. On the cool end ($G - G_{\text{RP}} \gtrsim 1.1$), Pleiades rotations are the fastest, as the ≈ 45 Myr stars are still contracting, although we have fewer period measurements for MUTA members in this regime. The overall trend is consistent with our assigned 61 ± 5 Myr age of MUTA based on empirical isochrones and the total age of the white dwarf WD 0340+103, though additional rotation period measurements would be useful to better map out its sequence.

Stellar rotation serves as a driver of magnetic activity through the dynamo effect (Reiners et al. 2012) and causes young stars to display enhanced UV and X-ray emission among other effects associated with an enhanced stellar activity (Kastner et al. 2003; Rodriguez et al. 2013; Malo et al. 2014a). We used data from the ROSAT all-sky survey (Boller et al. 2016) and the GALEX catalog (Martin et al. 2005) to verify that our population of MUTA members and candidates displays this expected enhanced activity in a way that is consistent with other young associations of similar ages (≈ 10 –150 Myr) in the solar neighborhood, including β PMG and the AB Doradus moving group (ABDMG; Zuckerman et al. 2004; see Gagné et al. 2018c for a discussion of these associations). The resulting distributions are shown in Figures 26 and 27 and provide more evidence that MUTA consists of a coeval and young association.

²² <https://github.com/afeinstein20/eleanor>

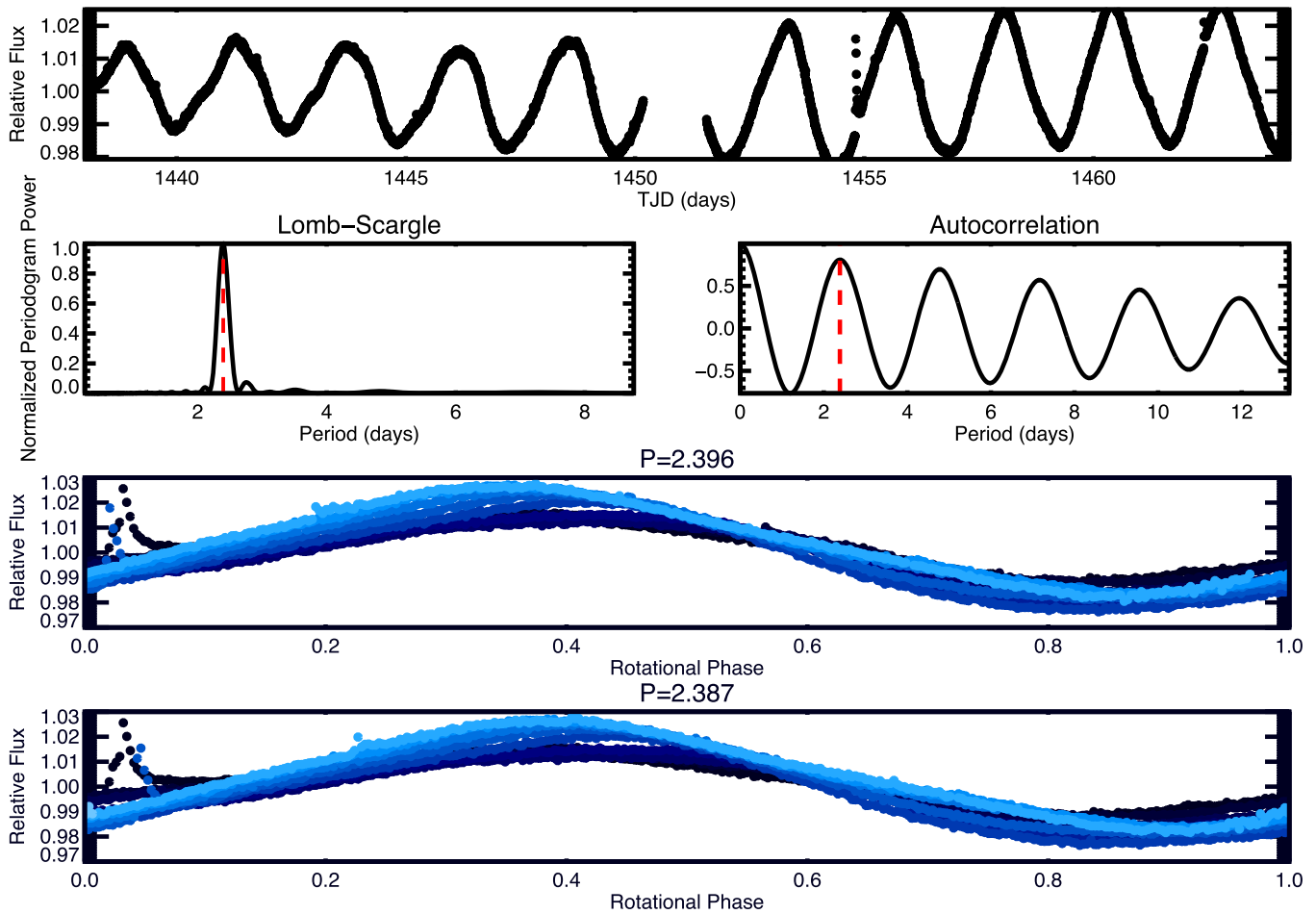


Figure 24. TESS light curve and rotation diagnostics of TIC178969585 (HD 29615), a G-type dwarf in the Tucana-Horologium association. The top panel shows the SPOC light curve, with the Lomb–Scargle power and autocorrelation function just below (the assigned period is marked with a red dashed line). The bottom two panels show the light curve phased to the period derived from the Lomb–Scargle (top) and autocorrelation function (bottom), color-coded by chronological order (lighter is later).

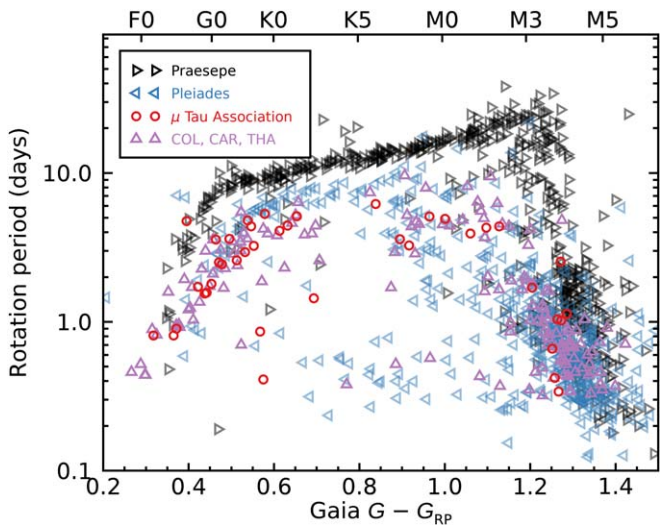


Figure 25. Rotation periods for stars in the Praesepe (black, ≈ 800 Myr) and Pleiades clusters (blue, ≈ 112 Myr); Columba (COL), Carina (CAR), or Tucana-Horologium (THA) associations (violet; ≈ 45 Myr); and MUTA (red; ≈ 60 Myr) as a function of Gaia $G - G_{RP}$ color.

6.8. μ Tau in the Context of the Galactic Structure

An unprecedented view of the local spatial and kinematic structure of the Galaxy was enabled with the advent of Gaia DR2. Using these new data, Kounkel & Covey (2019)

identified 1901 groups of stars that appear comoving and coeval, located within 30° of the Galactic plane and 1 kpc of the Sun. Their method used the HDBSCAN unsupervised clustering algorithm²³ directly in the five-dimensional parameter space of Gaia DR2 observables (sky position, proper motion, and parallax) to identify overdensities; this did not allow them to efficiently recover the structure within about 70 pc of the Sun because the large spread of nearby associations on the sky introduces strong variation and correlations in the Gaia DR2 five-dimensional kinematic space of the members within a specific young association. Kounkel & Covey (2019) separated the overdensities among clusters and strings, the latter consisting of much larger structures with typical physical sizes of about 200 pc and some of which also have extended kinematic distributions.

We cross-matched our sample of MUTA candidates and members with the full Kounkel & Covey (2019) catalog of clustered sources to determine whether MUTA had been recovered by their study. We found a total of 72 matches with our list, all with a single Kounkel & Covey (2019) string named Theia 160 that contains a total of 300 stars. Only four of these stars are matches to our initial list of MUTA members (HD 28715, HD 27687, HD 28356, and TYC 668-737-1; respectively, MUTA 11, 17, 18, and 30 A). One likely explanation for the partial overlap is the $|b| < 30^\circ$ cutoff in

²³ See <https://hdbscan.readthedocs.io>.

Table 11
TESS and K2 Rotation Periods

Name	R.A. (hh:mm:ss.sss)	Decl. (dd:mm:ss.ss)	Period 1 (days)	Period 2 ^a (days)	Young Association ^b	References
2MASS J03303685+1610599	03:30:36.887	+16:10:59.58	1.70	...	MUTA	2
2MASS J03350134+1418016	03:35:01.376	+14:18:01.14	4.38	...	MUTA	2
2MASS J03361762+2153391	03:36:17.665	+21:53:38.50	4.38	...	MUTA	2
2MASS J03371337+1307315	03:37:13.411	+13:07:30.93	0.66	...	MUTA	2
2MASS J03373508+1705162	03:37:35.111	+17:05:15.93	6.19	...	MUTA	2
RX J0338.3+1020	03:38:18.266	+10:20:16.32	3.24	...	MUTA	1
2MASS J03385230+1635406	03:38:52.328	+16:35:40.21	0.34	...	MUTA	2
TYC 1235-156-1	03:39:39.516	+15:29:54.47	4.43	...	MUTA	2
TYC 663-362-1	03:40:57.781	+13:09:03.06	2.59	...	MUTA	1
TYC 660-135-1	03:41:45.000	+10:54:27.46	5.12	...	MUTA	1
2MASS J03420359+1631392	03:42:03.617	+16:31:38.80	4.92	...	MUTA	2
HD 23376	03:44:58.957	+08:19:10.09	0.81	...	MUTA	1
BD+04 589	03:47:13.551	+05:26:23.49	4.75	...	MUTA	1

Notes. Rotation periods are accurate to approximately 2%. See Section 6.7 for more details.

^a Second rotation period candidate.

^b The full names of young associations are: Carina (CAR), Columba (COL), the Tucana-Horologium association (THA) and the μ Tau Association (MUTA).

References. (1) TESS (Ricker et al. 2015; Jenkins et al. 2016); (2) K2 (Borucki et al. 2010; Howell et al. 2014; Vanderburg & Johnson 2014).

(This table is available in its entirety in machine-readable form.)

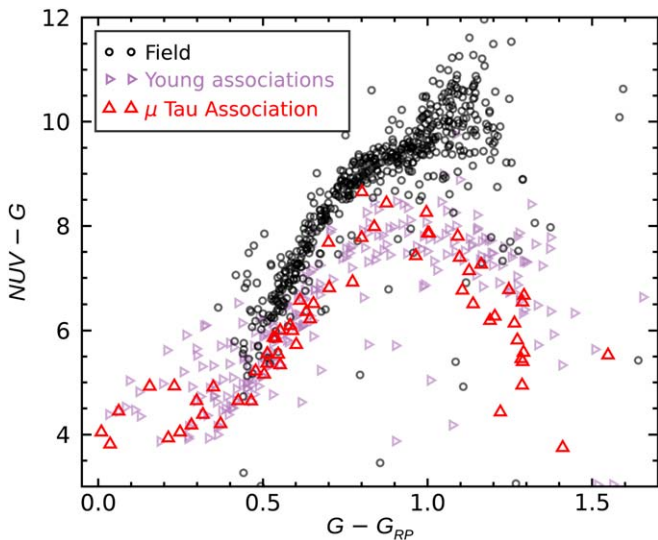


Figure 26. GALEX to Gaia DR2 $NUV - G$ color vs. $G - G_{RP}$ for field stars (black circles), members of nearby young associations (rightward-pointing purple triangles), and MUTA candidates studied in this paper (upward-pointing red triangles). Our candidates are consistent with the young stellar population displaying an NUV excess compared with field stars of the same $G - G_{RP}$ color. See Section 6.7 for more details.

Galactic latitude that they imposed, as approximately half of MUTA falls at $b < -30^\circ$. We show a comparison of Theia 160, MUTA, and Taurus in Figure 28. Theia 160 is spatially more extended but also shows a much larger spread in space velocities compared with MUTA, although Theia 160 members are centered at similar average velocities; MUTA members have a spread of (2.8, 2.1, 1.6) km s^{-1} in UVW space, whereas the spread of Theia 160 members is (21.1, 1.7, 8.9) km s^{-1} . This indicates that some interlopers may contaminate the sample of Theia 160 stars, and further investigation will be required to confirm this.

In addition to the similar kinematics between MUTA and Theia 160, Kounkel & Covey (2019) determined a model-

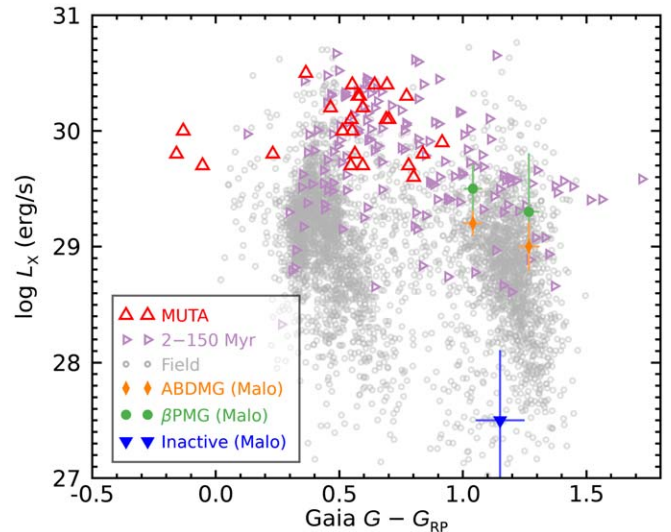


Figure 27. Absolute X-ray luminosity for field stars (gray circles), nearby young stars (rightward-pointing purple triangles), and our MUTA candidates (upward-pointing red triangles). The young M dwarf distributions of Malo et al. (2014a) are also shown for comparison. Young stars tend to emit more X-ray because they are more active. In the case of low-mass stars, this effect is compounded by the larger radius of younger M dwarfs. Field stars tend to be more active at both ends of the mass spectrum, consistent with their faster average rotation rates. β PMG indicates the β Pictoris moving group, and ABDMG indicates the AB Doradus moving group. See Section 6.7 for more details.

dependent isochronal age of $\simeq 80$ Myr for Theia 160, which is close to our estimated age of 61 ± 5 Myr. It seems likely that MUTA and Theia 160 are related to each other; perhaps Theia 160 represents a stream or tidal tail around the more closely packed core of MUTA (analogous to the tidal tail around the Hyades cluster, although the latter is much older; Röser et al. 2019), or it is simply a fragment of MUTA with some contaminating field stars that have more spread-out space velocities. Investigating this further will require a spectroscopic

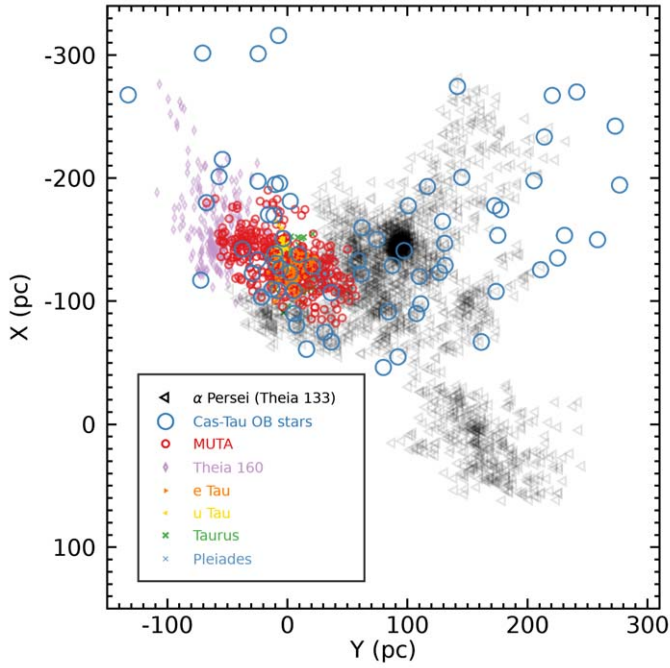
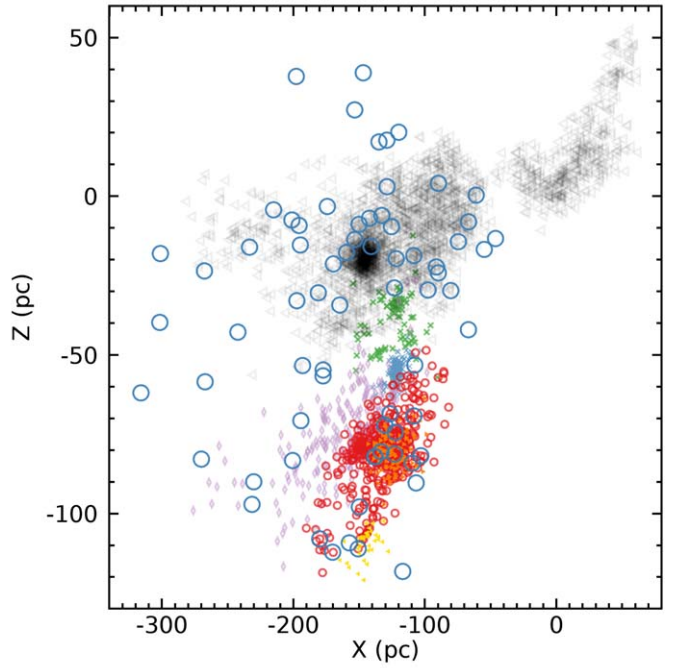
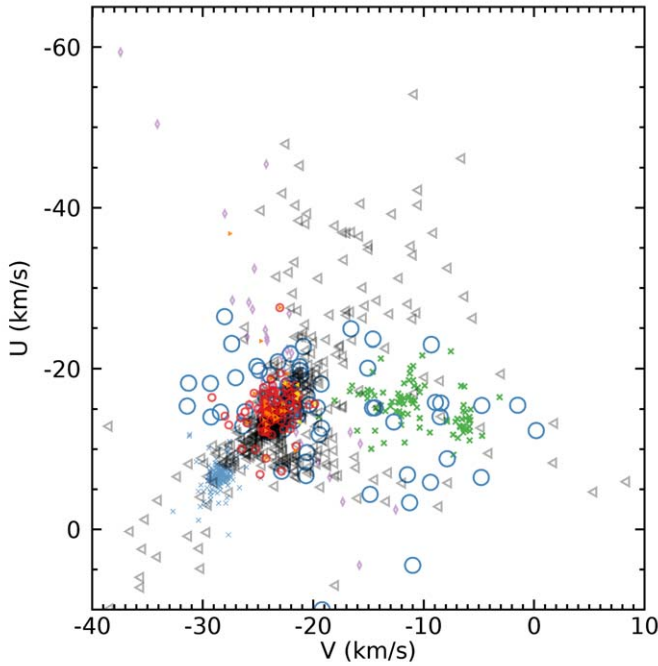
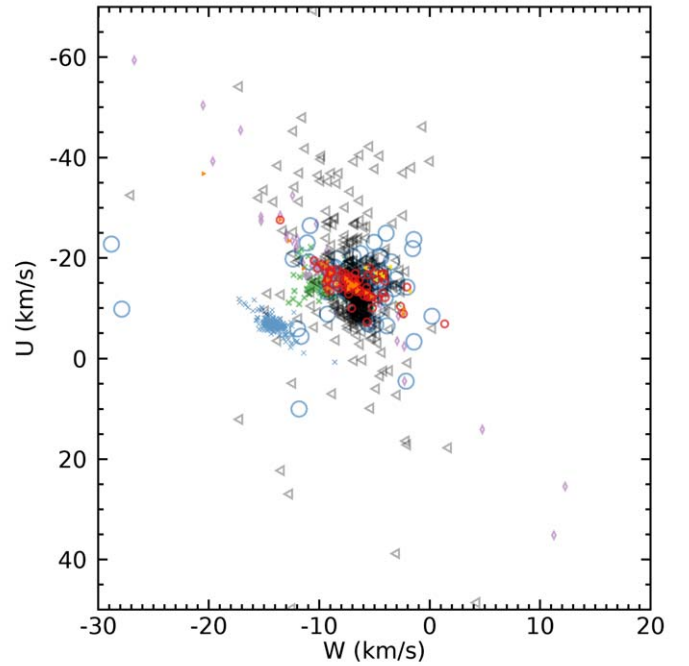
(a) Galactic positions X versus Y (b) Galactic positions X versus Z (c) Space velocities U versus V (d) Space velocities U versus W

Figure 28. Spatial and kinematic distribution of MUTA candidates and members discussed in this work (red circles), compared with the neighbor Taurus association (rightward-pointing green triangles) and the Theia 160 kinematic string (blue diamonds). The similar kinematics and isochronal ages of Theia 160 and MUTA indicate that these two Galactic structures may be related to one another. See Section 6.8 for more details.

follow-up of candidates in both MUTA and Theia 160 to complete the UVW measurements of all members in both groups—although the next data release of the Gaia DR2 mission will likely allow us to complete the UVW velocities of most MUTA members and determine spectroscopic signs of young ages. It is possible that our method did not recover the full spatial structure of MUTA, especially regions that would lack massive stars, because BANYAN Σ requires an initial

kinematic model to work with, which we obtained from the initial collection of young or active stars described in Section 2. In addition to this, Kounkel & Covey (2019) uncovered a large kinematic structure (Theia 133) that encompasses the α Persei cluster, likely related to Cas-Tau and MUTA, as discussed in Section 2. This structure is also shown in Figure 28.

Liu et al. (2020) recently published the discovery of two new associations physically nearby (but unrelated to) the Taurus-

Table 12
Main List of All Systems of Interest to MUTA Identified in This Work

Name	Units	Type	Format	Description
MUTA	...	char	A6	μ Tau Association (MUTA) identification number.
Name	...	char	A28	Main target name. SIMBAD-resolvable names are preferred; short names in the format J0236+2026 are given otherwise.
Gaia	...	char	A19	Gaia DR2 identification number.
2MASS	...	char	A16	2MASS designation.
AllWISE	...	char	A19	AllWISE designation.
ROSAT	...	char	A16	ROSAT designation.
Tycho	...	char	A11	Tycho catalog designation.
Hipparcos	...	int	I5	Hipparcos catalog designation.
SIMBAD	...	char	A24	Principal SIMBAD identifier.
SpT	...	char	A11	Literature spectral type. Spectral type estimates based on Gaia DR2 colors are given between parentheses. (WD) indicates likely white dwarfs.
r_SpT	...	char	A19	Reference for literature spectral type.
Memb-Type	...	char	A2	Membership type. IM: member from our initial list. CM: candidate member. LM: low-priority candidate member. R: rejected candidate member.
Source	...	char	A14	Source from which the target was obtained. INIT: initial list described in Section 2. GAIA: originates from our Gaia DR2-based search for additional candidate members described in Section 4. COM: originates from our comover search described in Section 4.1. VIS: originates from our visual identification of comover candidates described in Section 4.5. OH2017: originates from an Oh et al. (2017) group with a partial match to our MUTA members and candidates.
Memb-Prob	%	R*4	F5.1	BANYAN Σ probability for membership in MUTA.
UVW-sep	km s ⁻¹	R*4	F4.1	Smallest possible separation from the center of the BANYAN Σ model in <i>UVW</i> space.
XYZ-sep	km s ⁻¹	R*4	F5.1	Smallest possible separation from the center of the BANYAN Σ model in <i>XYZ</i> space.
ra	h:m:s			Gaia DR2 R.A. (J2000) at epoch 2015.5 in the ICRS reference frame.
dec	d:m:s			Gaia DR2 decl. (J2000) at epoch 2015.5 in the ICRS reference frame.
pmRA	mas yr ⁻¹	R*4	F6.3	Gaia DR2 proper motion in R.A., including the $\cos \delta$ Jacobian term.
pmDE	mas yr ⁻¹	R*4	F7.3	Gaia DR2 proper motion in decl.
e_pmRA	mas yr ⁻¹	R*4	F5.3	Measurement error for Gaia DR2 proper motion in R.A.
e_pmDE	mas yr ⁻¹	R*4	F5.3	Measurement error for Gaia DR2 proper motion in decl.
plx	mas	R*4	F5.2	Gaia DR2 parallax.
e_plx	mas	R*4	F4.2	Measurement error for Gaia DR2 parallax.
ruwe	...	R*4	F4.1	Renormalized unit weight error of the Gaia DR2 astrometric solution. See Section 4.4 for more details.
RV	km s ⁻¹	R*4	F4.1	Radial velocity measurement from the literature.
e_RV	km s ⁻¹	R*4	F4.1	Measurement error for radial velocity measurement.
r_RV	...	char	A19	Reference for literature radial velocity measurement.
Pred-RV	km s ⁻¹	R*4	I2	Predicted radial velocity that maximizes MUTA membership probability obtained from BANYAN Σ , only listed for targets without a radial velocity measurement.
e_Pred-RV	km s ⁻¹	int	I1	1σ confidence range on predicted radial velocity that maximizes MUTA membership probability.
Gmag	mag	R*8	F7.4	Gaia DR2 <i>G</i> -band magnitude.
e_Gmag	mag	R*8	F6.4	Measurement error for Gaia DR2 <i>G</i> -band magnitude.
RPmag	mag	R*4	F7.4	Gaia DR2 <i>G</i> _{RP} -band magnitude.
e_RPmag	mag	R*4	F6.4	Measurement error for Gaia DR2 <i>G</i> _{RP} -band magnitude.
BPmag	mag	R*4	F7.4	Gaia DR2 <i>G</i> _{BP} -band magnitude.
e_BPmag	mag	R*4	F6.4	Measurement error for Gaia DR2 <i>G</i> _{BP} -band magnitude.
Jmag	mag	R*4	F6.3	2MASS <i>J</i> -band magnitude.
e_Jmag	mag	R*4	F5.3	Measurement error for 2MASS <i>J</i> -band magnitude.
Hmag	mag	R*4	F6.3	2MASS <i>H</i> -band magnitude.
e_Hmag	mag	R*4	F5.3	Measurement error for 2MASS <i>H</i> -band magnitude.
Ksmag	mag	R*4	F6.3	2MASS <i>K</i> _S -band magnitude.
e_Ksmag	mag	R*4	F5.3	Measurement error for 2MASS <i>K</i> _S -band magnitude.
W1mag	mag	R*4	F5.2	AllWISE W1-band magnitude, W1MPRO entry in the original catalog.
e_W1mag	mag	R*4	F4.2	Measurement error for AllWISE W1-band magnitude, W1SIGMPRO entry in the original catalog.
W2mag	mag	R*4	F5.2	AllWISE W2-band magnitude, W2MPRO entry in the original catalog.
e_W2mag	mag	R*4	F4.2	Measurement error for AllWISE W2-band magnitude, W2SIGMPRO entry in the original catalog.
W3mag	mag	R*4	F5.2	AllWISE W3-band magnitude, W3MPRO entry in the original catalog.
e_W3mag	mag	R*4	F4.2	Measurement error for AllWISE W3-band magnitude, W3SIGMPRO entry in the original catalog.
E(B-V)	mag	R*4	F4.2	$E(B - V)$ reddening based on the STILISM reddening map combined with Gaia DR2 distance and sky position. See Section 5 for more details.
e_E(B-V)	mag	R*4	F4.2	Measurement error for $E(B - V)$ reddening.
NUVmag	mag	R*4	F6.3	GALEX NUV-band magnitude.
e_NUVmag	mag	R*4	F5.3	Measurement error for GALEX NUV-band magnitude.
FUVmag	mag	R*4	F6.3	GALEX FUV-band magnitude.
e_FUVmag	mag	R*4	F5.3	Measurement error for GALEX FUV-band magnitude.

Table 12
(Continued)

Name	Units	Type	Format	Description
HR1	...	R*4	F5.2	ROSAT hardness ratio HR1.
HR2	...	R*4	F5.2	ROSAT hardness ratio HR2.
XrayFlux	ct/s	R*4	F4.2	ROSAT X-ray counts.
e_XrayFlux	ct/s	R*4	F4.2	Measurement error for ROSAT X-ray counts.
logLX	...	R*4	F4.1	Absolute X-ray luminosity $\log L_X/L_\odot$ calculated from ROSAT X-ray data and Gaia DR2 trigonometric distance.
e_logLX	...	R*4	F3.1	Measurement error for absolute X-ray luminosity.
EW	mÅ	int	I3	Lithium absorption-line equivalent width.
r_EW	...	char	A19	Reference for lithium absorption-line equivalent width.
Teff	K	int	I4	Effective temperature.
r_Teff	...	char	A19	Reference for effective temperature.
Primary	...	int	I1	1: single stars or primary (brightest) star in a multiple system. 0: companion star in a multiple system.
Multi	...	char	A2	Identifier letter for multiple system components.
Sep	arcsec	R*8	F8.4	Separation from primary star calculated from Gaia DR2 positions.
e_Sep	arcsec	R*8	F6.4	Measurement error for separation.
PA	deg	R*8	F8.4	Position angle with respect to primary star calculated from Gaia DR2 positions.
e_PA	deg	R*8	F6.4	Measurement error for position angle.
Comover-Gaia	...	char	A79	Gaia DR2 identification number for comoving star (primary or companion). Multiple entries are separated by a semicolon.
Oh2017Group	...	int	I4	Comoving group identification number from Oh et al. (2017).

(This table is available in its entirety in machine-readable form.)

Auriga star-forming region; e Tau and u Tau. The group that they identified as e Tau has significant overlap with our definition of MUTA; 104 of their 119 members are also in our list (18 in our initial members, 79 in our candidate members, 6 in our low-likelihood candidate members, and 1 in our list of rejected members). The 15 remaining objects not in our catalogs that they list as e Tau members have either a Bayesian membership probability below 90% or a best-case scenario separation above 5 km s^{-1} with our kinematic model, which explains why we have not recovered them. We identified in this paper a total of 444 candidate members that Liu et al. (2020) did not discuss: 18 in our initial members, 277 candidate members, and 149 in our low-likelihood candidate members. An additional 12 objects in our MUTA lists (4 initial members, 6 candidate members, and 2 low-likelihood candidates) are listed as u Tau members by Liu et al. (2020). The isochrone age of $\simeq 50$ Myr determined by Liu et al. (2020) is similar to our 61 ± 5 Myr but is based on model isochrones rather than empirical ones.

The fact that Kounkel & Covey (2019) and Liu et al. (2020) may have uncovered spatial extensions of MUTA, as well as the presence of a large structure of additional stars coeval with MUTA and α Persei, hints that it would be valuable to parse the local solar neighborhood with an overdensity detection algorithm that is not hindered by the lack of radial velocity measurements or the large spread and correlations of sky positions, proper motions, and parallaxes of nearby cluster members. Such a study would have the potential to uncover extended structures and connections between the Kounkel & Covey (2019) groups and the known nearby young associations in the solar neighborhood, as well as new nearby associations entirely.

7. Conclusions

We presented and characterized the μ Tau Association, a young stellar population consisting of hundreds of members at

about 150 pc from the Sun. We built a BANYAN Σ spatial-kinematic model for this association to identify additional candidate members with Gaia DR2 and to allow other teams to search for new members. The Gaia DR2 photometry and parallaxes of MUTA members allowed us to make a comparison with empirical sequences of the Pleiades, Tucana-Horologium, Carina, and Columba members to determine an isochronal age relative to these other young associations. This resulted in an age estimate of 62 ± 7 Myr for MUTA. We identified a white dwarf (WD 0340+103) that is the remnant of a B2 MUTA member that left its planetary nebula phase 270,000 yr ago and used its total age to further constrain the age of MUTA at 61 ± 5 Myr. We found literature measurements of the lithium equivalent width for K-type to G-type members of MUTA and showed that they are consistent with our age determination. The members of this new association have a Gaia DR2 color versus TESS rotation period sequence consistent with a young age and display an enhanced level of stellar activity compared with the field population based on UV and X-ray, consistent with a young coeval population. We also showed that its present-day mass function is similar to other known young associations. MUTA is likely part of an extended network of stars coeval and comoving with the α Persei cluster that are currently dissolving. A master table with all candidates and members of the MUTA association is also provided here (Table 12).

The MUTA association is a new laboratory to study stellar and exoplanet evolution at an age that was not well sampled by other associations within the solar neighborhood. Its distance of $\simeq 150$ pc will make it harder to identify its substellar population, but upcoming wide-area surveys such as Pan-STARRS 3π (Magnier et al. 2010) and CatWISE (Eisenhardt et al. 2020) may be able to do so in the near future. The extended ROentgen Survey with an Imaging Telescope Array (eROSITA; Predehl et al. 2014) on the Spektrum-Roentgen-Gamma (SRG) space telescope will also likely allow us to better study the activity of the low-mass stars in MUTA.

We thank the anonymous reviewer for thoughtful and constructive comments. We thank Patrick Dufour, Aaron Rizzuto, and Benjamin Tofflemire for useful comments. We thank Za Gurēto Muta for guidance in choosing an acronym for the μ Tau Association. This work was partially carried under a Banting grant from the Natural Sciences and Engineering Research Council of Canada (NSERC). This research made use of the SIMBAD database and VizieR catalog access tool, operated at the Centre de Données astronomiques de Strasbourg, France (Ochsenbein et al. 2000); data products from the Two Micron All Sky Survey (2MASS; Skrutskie et al. 2006), which is a joint project of the University of Massachusetts and the Infrared Processing and Analysis Center (IPAC)/California Institute of Technology (Caltech), funded by the National Aeronautics and Space Administration (NASA) and the National Science Foundation (Skrutskie et al. 2006); and data products from the Wide-field Infrared Survey Explorer (WISE; and Wright et al. 2010), which is a joint project of the University of California, Los Angeles, and the Jet Propulsion Laboratory (JPL)/Caltech, funded by NASA. The Digitized Sky Surveys (DSS) were produced at the Space Telescope Science Institute under U.S. Government grant NAG W-2166. The images of these surveys are based on photographic data obtained using the Oschin Schmidt Telescope on Palomar Mountain and the UK Schmidt Telescope. The plates were processed into the present compressed digital form with the permission of these institutions. The Second Palomar Observatory Sky Survey (POSS-II) was made by the California Institute of Technology with funds from the National Science Foundation, the National Geographic Society, the Sloan Foundation, the Samuel Oschin Foundation, and the Eastman Kodak Corporation. The Oschin Schmidt Telescope is operated by the California Institute of Technology and Palomar Observatory. This work presents results from the European Space Agency (ESA) space mission Gaia. Gaia data are being processed by the Gaia Data Processing and Analysis Consortium (DPAC). Funding for the DPAC is provided by national institutions, in particular the institutions participating in the Gaia MultiLateral Agreement (MLA). The Gaia mission website is <https://www.cosmos.esa.int/gaia>. The Gaia archive website is <https://archives.esac.esa.int/gaia>. The Digitized Sky Surveys were produced at the Space Telescope Science Institute under U.S. Government grant NAG W-2166. Part of this research was carried out at the Jet Propulsion Laboratory, California Institute of Technology, under a contract with the National Aeronautics and Space Administration (80NM0018D0004). T.J.D. and E.E.M. gratefully acknowledge support from the Jet Propulsion Laboratory Exoplanetary Science Initiative and NASA award 17-K2GO6-0030. E.E.M. acknowledges support from NASA grant NNX15AD53G.

J.G. wrote the codes and manuscript, generated figures, and led the analysis; T.J.D. compiled an initial list of new candidates and generated Figure 1; E.E.M. first identified the overdensity associated with MUTA, led the turnoff age analysis and the investigation of HD 27860, and provided the initial member list; A.W.M. led the rotation periods analysis, wrote part of Section 6.7, and built Figures 24 and 25; J.K.F. provided help with parsing the Gaia DR2 data and general comments; and A.B. provided the atmosphere analysis of WD 0340+103 and Figure 21.

Software: BANYAN Σ (Gagné et al. 2018c), Eleanor (Feinstein et al. 2019).

ORCID iDs

Jonathan Gagné  <https://orcid.org/0000-0002-2592-9612>
 Trevor J. David  <https://orcid.org/0000-0001-6534-6246>
 Eric E. Mamajek  <https://orcid.org/0000-0003-2008-1488>
 Andrew W. Mann  <https://orcid.org/0000-0003-3654-1602>
 Jacqueline K. Faherty  <https://orcid.org/0000-0001-6251-0573>
 Antoine Bédard  <https://orcid.org/0000-0002-2384-1326>

References

- Abt, H. A. 2008, *ApJS*, 176, 216
- Ahn, C. P., Alexandroff, R., Allende Prieto, C., et al. 2012, *ApJS*, 203, 21
- Alam, S., Albareti, F. D., Allende Prieto, C., et al. 2015, *ApJS*, 219, 12
- Allard, F., Homeier, D., & Freytag, B. 2012, *RSPTA*, 370, 2765
- Avvakumova, E. A., Malkov, O. Y., & Kniazev, A. Y. 2013, *AN*, 334, 860
- Babusiaux, C., van Leeuwen, F., Barstow, M., et al. 2018, *A&A*, 616, A10
- Bai, Y., Liu, J., Bai, Z., Wang, S., & Fan, D. 2019, *AJ*, 158, 93
- Baraffe, I., Homeier, D., Allard, F., & Chabrier, G. 2015, *A&A*, 577, A42
- Barnes, S. A. 2003, *ApJ*, 586, 464
- Barrado y Navascués, D., García López, R. J., Severino, G., & Gomez, M. T. 2001, *A&A*, 371, 652
- Barrado y Navascués, D., Stauffer, J. R., & Jayawardhana, R. 2004, *ApJ*, 614, 386
- Beavers, W. I., & Cook, D. B. 1980, *ApJS*, 44, 489
- Bédard, A., Bergeron, P., Brassard, P., & Fontaine, G. 2020, *ApJ*, 901, 93
- Bell, C. P. M., Mamajek, E. E., & Naylor, T. 2015, *MNRAS*, 454, 593
- Bergeron, P., Saffer, R. A., & Liebert, J. 1992, *ApJ*, 394, 228
- Bergeron, P., Wesemael, F., Dufour, P., et al. 2011, *ApJ*, 737, 28
- Bertelli, G., Nasi, E., Girardi, L., & Marigo, P. 2009, *A&A*, 508, 355
- Bidelman, W. P., Ratcliff, S. J., & Svolopoulos, S. 1988, *PASP*, 100, 828
- Blaauw, A. 1956, *ApJ*, 123, 408
- Bochanski, J. J., Hawley, S. L., Covey, K. R., et al. 2010, *AJ*, 139, 2679
- Boller, T., Freyberg, M. J., Trümper, J., et al. 2016, *A&A*, 588, A103
- Borucki, W. J., Koch, D., Basri, G., et al. 2010, *Sci*, 327, 977
- Bouvier, J., Barrado, D., Moraux, E., et al. 2018, *A&A*, 613, A63
- Bouy, H., Bertin, E., Barrado, D., et al. 2015, *A&A*, 575, A120
- Brandt, T. D., & Huang, C. X. 2015, *ApJ*, 807, 24
- Burke, C. J., Pinsonneault, M. H., & Sills, A. 2004, *ApJ*, 604, 272
- Camisassa, M. E., Althaus, L. G., Córscico, A. H., et al. 2019, *A&A*, 625, A87
- Cannon, A. J., & Pickering, E. C. 1993, *yCat*, 3135
- Capitania, L., Lallement, R., Vergely, J. L., Elyajouri, M., & Monreal-Ibero, A. 2017, *A&A*, 606, A65
- Chambers, K. C., Magnier, E. A., & Metcalfe, N. 2016, arXiv:1612.05560
- Choi, J., Dotter, A., Conroy, C., et al. 2016, *ApJ*, 823, 102
- Cowley, A. 1968, *PASP*, 80, 453
- Cowley, A. 1972, *AJ*, 77, 750
- Cowley, A., Cowley, C., Jaschek, M., & Jaschek, C. 1969, *AJ*, 74, 375
- Cropper, M., Katz, D., Sartoretto, P., et al. 2018, *A&A*, 616, A5
- Curtis, J. L., Agüeros, M. A., Mamajek, E. E., Wright, J. T., & Cummings, J. D. 2019, *AJ*, 158, 77
- Dahn, S. E. 2015, *ApJ*, 813, 108
- de Zeeuw, P. T., Hoogerwerf, R., de Bruijne, J. H. J., Brown, A. G. A., & Blaauw, A. 1999, *AJ*, 117, 354
- Delorme, P., Collier Cameron, A., Hebb, L., et al. 2011, *MNRAS*, 413, 2218
- Dobbie, P. D., Lodieu, N., & Sharp, R. G. 2010, *MNRAS*, 409, 1002
- Douglas, S. T., Agüeros, M. A., Covey, K. R., et al. 2016, *ApJ*, 822, 47
- Douglas, S. T., Agüeros, M. A., Covey, K. R., & Kraus, A. 2017, *ApJ*, 842, 83
- Dupuy, T. J., & Liu, M. C. 2012, *ApJS*, 201, 19
- Eisenhardt, P. R. M., Marocco, F., Fowler, J. W., et al. 2020, *ApJS*, 247, 69
- ESA 1997, The Hipparcos and Tycho Catalogs. Astrometric and Photometric Star Catalogs Derived from the ESA Hipparcos Space Astrometry Mission (Noordwijk: ESA)
- Evans, D. S. 1967, in IAU Symp. 30, Determination of Radial Velocities and their Applications, ed. A. H. Batten & J. F. Heard (Toronto: Academic), 57
- Evans, D. W., Riello, M., & De Angeli, F. 2018a, arXiv:1804.09368
- Evans, D. W., Riello, M., De Angeli, F., et al. 2018b, *A&A*, 616, A4
- Faherty, J. K., Bochanski, J. J., Gagné, J., et al. 2018, *ApJ*, 863, 91
- Faherty, J. K., Riedel, A. R., Cruz, K. K., et al. 2016, *ApJS*, 225, 10
- Feinstein, A. D., Montet, B. T., Foreman-Mackey, D., et al. 2019, *PASP*, 131, 094502
- Filippazzo, E. L. 1999, *PASP*, 111, 63
- Filippazzo, J. C., Rice, E. L., Faherty, J., et al. 2015, *ApJ*, 810, 158
- Flower, P. J. 1996, *ApJ*, 469, 355

- Fontaine, G., Brassard, P., & Bergeron, P. 2001, *PASP*, **113**, 409
- Gaia Collaboration, Brown, A. G. A., Vallenari, A., et al. 2018, *A&A*, **616**, A1
- Gagné, J., & Faherty, J. K. 2018, *ApJ*, **862**, 138
- Gagné, J., Faherty, J. K., Cruz, K. L., et al. 2015, *ApJS*, **219**, 33
- Gagné, J., Faherty, J. K., & Mamajek, E. E. 2018a, *ApJ*, **865**, 136
- Gagné, J., Fontaine, G., Simon, A., & Faherty, J. K. 2018b, *ApJL*, **861**, L13
- Gagné, J., Lafrenière, D., Doyon, R., Malo, L., & Artigau, É. 2014, *ApJ*, **783**, 121
- Gagné, J., Mamajek, E. E., Malo, L., et al. 2018c, *ApJ*, **856**, 23
- Gagné, J., Roy-Loubier, O., Faherty, J. K., Doyon, R., & Malo, L. 2018d, *ApJ*, **860**, 43
- Gagné, J., Schneider, A., & Cushing, M. 2018e, Finder Charts Python Package v1.0, Zenodo, doi:10.5281/zenodo.1237017
- Gentile Fusillo, N. P., Tremblay, P.-E., Gänsicke, B. T., et al. 2019, *MNRAS*, **482**, 4570
- Gontcharov, G. A. 2006, *AstL*, **32**, 759
- Gray, R. O., Corbally, C. J., Garrison, R. F., et al. 2006, *AJ*, **132**, 161
- Gray, R. O., Corbally, C. J., Garrison, R. F., McFadden, M. T., & Robinson, P. E. 2003, *AJ*, **126**, 2048
- Grenier, S., Baylac, M. O., Rolland, L., et al. 1999, *A&AS*, **137**, 451
- Gullikson, K., Kraus, A. L., & Dodson-Robinson, S. 2016, *AJ*, **152**, 40
- Hambly, N. C., Cropper, M., Boudreault, S., et al. 2018, *A&A*, **616**, A15
- Heckmann, O., & Lübeck, K. 1958, *ZA*, **45**, 243
- Hohle, M. M., Neuhauser, R., & Schutz, B. F. 2010, *AN*, **331**, 349
- Holberg, J. B., & Bergeron, P. 2006, *AJ*, **132**, 1221
- Hollands, M. A., Tremblay, P. E., Gänsicke, B. T., Gentile-Fusillo, N. P., & Toonen, S. 2018, *MNRAS*, **480**, 3942
- Home, J. H., & Baliunas, S. L. 1986, *ApJ*, **302**, 757
- Howell, S. B., Sobek, C., Haas, M., et al. 2014, *PASP*, **126**, 398
- Jaschek, M., & Jaschek, C. 1980, *A&AS*, **42**, 115
- Jeffries, R. D. 2012, in *EAS Publications Series 57, Low-Mass Stars and the Transition Stars/Brown Dwarfs—EES2011*, ed. C. Reylé et al. (EDP Sciences: Les Ulis), 45
- Jenkins, J. M., Twicken, J. D., McCaulliff, S., et al. 2016, *Proc. SPIE*, **9913**, 99133E
- Jones, B. F., Fischer, D., & Soderblom, D. R. 1999, *AJ*, **117**, 330
- Jones, B. F., Shetrone, M., Fischer, D., & Soderblom, D. R. 1996, *AJ*, **112**, 186
- Kastner, J. H., Crigger, L., Rich, M., & Weintraub, D. A. 2003, *ApJ*, **585**, 878
- Kenyon, S. J., Gómez, M., & Whitney, B. A. 2008, in *Handbook of Star-forming Regions*, ed. B. Reipurth, Vol. 1 (San Francisco, CA: ASP), 405
- Kharchenko, N. V., Scholz, R. D., Piskunov, A. E., Röser, S., & Schilbach, E. 2007, *AN*, **328**, 889
- Kirkpatrick, D. J., Cushing, M. C., Cruz, K. K., et al. 2011, *ApJS*, **197**, 19
- Kirkpatrick, D. J., Gelino, C. R., Cushing, M. C., et al. 2012, *ApJ*, **753**, 156
- Kleinman, S. J., Kepler, S. O., Koester, D., et al. 2013, *ApJS*, **204**, 5
- Koukkel, M., & Covey, K. 2019, *AJ*, **158**, 122
- Kowalski, P. M., & Saumon, D. 2006, *ApJL*, **651**, L137
- Kraus, A. L., Shkolnik, E. L., Allers, K. N., & Liu, M. C. 2014, *AJ*, **147**, 146
- Lallement, R., Capitanio, L., Ruiz-Dern, L., et al. 2018, *A&A*, **616**, A132
- Lallement, R., Vergely, J. L., Valette, B., et al. 2014, *A&A*, **561**, A91
- Lauffer, G. R., Romero, A. D., & Kepler, S. O. 2018, *MNRAS*, **480**, 1547
- Lawrence, A., Warren, S. J., Almaini, O., et al. 2007, *MNRAS*, **379**, 1599
- Lesh, J. R. 1968, *ApJS*, **17**, 371
- Liebert, J., Bergeron, P., & Holberg, J. B. 2005, *ApJS*, **156**, 47
- Lindgren, L., Hernández, J., Bombrun, A., et al. 2018, *A&A*, **616**, A2
- Liu, J., Fang, M., & Liu, C. 2020, *AJ*, **159**, 105
- Liu, M. C., Dupuy, T. J., & Allers, K. N. 2016, *ApJ*, **833**, 96
- Lodieu, N., Pérez-Garrido, A., Smart, R. L., & Silvotti, R. 2019, *A&A*, **628**, A66
- Luhman, K. L. 2018, *AJ*, **156**, 271
- Luri, X., A Brown, A. G., Sarro, L., et al. 2018, *A&A*, **616**, A9
- Mace, G. N. 2014, PhD thesis, University of California
- Magazzù, A., Martín, E. L., Sterzik, M. F., et al. 1997, *A&AS*, **124**, 449
- Magnier, E. A., Liu, M., Goldman, B., et al. 2010, *HiA*, **15**, 818
- Makarov, V. V., & Urban, S. 2000, *MNRAS*, **317**, 289
- Malo, L., Artigau, É., Doyon, R., et al. 2014a, *ApJ*, **788**, 81
- Malo, L., Doyon, R., Feiden, G. A., et al. 2014b, *ApJ*, **792**, 37
- Malo, L., Doyon, R., Lafrenière, D., et al. 2013, *ApJ*, **762**, 88
- Mamajek, E. E. 2005, *ApJ*, **634**, 1385
- Martin, D. C., Fanson, J., Schiminovich, D., et al. 2005, *ApJL*, **619**, L1
- Mason, B. D., Wycoff, G. L., Hartkopf, W. I., Douglass, G. G., & Worley, C. E. 2001, *AJ*, **122**, 3466
- McMahon, R. G., Banerji, M., Gonzalez, E., et al. 2013, *Msngr*, **154**, 35
- McQuillan, A., Aigrain, S., & Mazeh, T. 2013, *MNRAS*, **432**, 1203
- Meingast, S., Alves, J., & Fürnkranz, V. 2019, *A&A*, **622**, L13
- Mentuch, E., Brandeker, A., van Kerkwijk, M. H., Jayawardhana, R., & Hauschildt, P. H. 2008, *ApJ*, **689**, 1127
- Mignard, F., Klioner, S., Lindgren, L., et al. 2018, *A&A*, **616**, A14
- Molnar, M. R. 1972, *ApJ*, **175**, 453
- Nesterov, V. V., Kuzmin, A. V., Ashimbaeva, N. T., et al. 1995, *A&A*, **110**, 367
- Neuhaeuser, R., Sterzik, M. F., Schmitt, J. H. M. M., Wichmann, R., & Krautter, J. 1995, *A&A*, **295**, L5
- Ochsenbein, F., Bauer, P., & Marcout, J. 2000, *A&AS*, **143**, 23
- Oh, S., Price-Whelan, A. M., Hogg, D. W., Morton, T. D., & Spergel, D. N. 2017, *AJ*, **153**, 257
- Pecaut, M. J., & Mamajek, E. E. 2013, *ApJS*, **208**, 9
- Perryman, M. A. C., Brown, A. G. A., Lebreton, Y., et al. 1998, *A&A*, **331**, 81
- Perryman, M. A. C., Lindgren, L., Kovalevsky, J., et al. 1997, *A&A*, **323**, L49
- Pickles, A. J. 1998, *PASP*, **110**, 863
- Predehl, P., Andritschke, R., Becker, W., et al. 2014, *Proc. SPIE*, **9144**, 91441T
- Randich, S. 2001, *A&A*, **377**, 512
- Rasmuson, N. H. 1921, *MeLus*, **26**, 3
- Rebull, L. M., Stauffer, J. R., Bouvier, J., et al. 2016, *AJ*, **152**, 113
- Reiners, A., Joshi, N., & Goldman, B. 2012, *AJ*, **143**, 93
- Reino, S., de Bruijne, J., Zari, E., d'Antona, F., & Ventura, P. 2018, *MNRAS*, **477**, 3197
- Ricker, G. R., Winn, J. N., Vanderspek, R., et al. 2015, *JATIS*, **1**, 014003
- Riedel, A. R., Blunt, S. C., Lambrides, E. L., et al. 2017, *AJ*, **153**, 95
- Riello, M., De Angeli, F., Evans, D. W., et al. 2018, *A&A*, **616**, A3
- Rodriguez, D. R., Zuckerman, B., Kastner, J. H., et al. 2013, *ApJ*, **774**, 101
- Röser, S., & Schilbach, E. 2019, *A&A*, **627**, A4
- Röser, S., Schilbach, E., & Goldman, B. 2019, *A&A*, **621**, L2
- Sartoretti, P., Katz, D., Cropper, M., et al. 2018, *A&A*, **616**, A6
- Shkolnik, E. L., Allers, K. N., Kraus, A. L., Liu, M. C., & Flagg, L. 2017, *AJ*, **154**, 69
- Simon, A. 2018, PhD thesis, Université de Montréal
- Simon, A., Fontaine, G., & Brassard, P. 2015, in *ASP Conf. Series 493, 19th European Workshop on White Dwarfs*, ed. P. Dufour et al. (San Francisco, CA: ASP), 137
- Skrutskie, M. F., Cutri, R. M., Stiening, R., et al. 2006, *AJ*, **131**, 1163
- Smart, R. L., Marocco, F., Sarro, L. M., et al. 2019, *MNRAS*, **485**, 4423
- Soderblom, D. R., Jones, B. F., Balachandran, S., et al. 1993, *AJ*, **106**, 1059
- Soubiran, C., Jasniewicz, G., Chemin, L., et al. 2018, *A&A*, **616**, A7
- Tang, S.-Y., Pang, X., Yuan, Z., et al. 2019, *ApJ*, **877**, 12
- Torres, C. A. O., da Silva, L., Quast, G. R., de la Reza, R., & Jilinski, E. 2000, *AJ*, **120**, 1410
- Torres, C. A. O., Quast, G. R., da Silva, L., et al. 2006, *A&A*, **460**, 695
- Torres, C. A. O., Quast, G. R., Melo, C. H. F., & Sterzik, M. F. 2008, in *Handbook of Star Forming Regions*, ed. B. Reipurth, Vol. 2 (San Francisco, CA: ASP), 757
- Tremblay, P. E., Bergeron, P., & Gianninas, A. 2011, *ApJ*, **730**, 128
- van Leeuwen, F. 2007, *A&A*, **474**, 653
- van Saders, J. L., Ceillier, T., Metcalfe, T. S., et al. 2016, *Natur*, **529**, 181
- Vanderburg, A., & Johnson, J. A. 2014, *PASP*, **126**, 948
- White, R. J., Gabor, J. M., & Hillenbrand, L. A. 2007, *AJ*, **133**, 2524
- Wichmann, R., Torres, G., Melo, C. H. F., et al. 2000, *A&A*, **359**, 181
- Wilson, R. E. 1953, *General Catalogue of Stellar Radial Velocities* (Washington, DC: Carnegie Institution of Washington)
- Woolley, R., Penston, M. J., Harding, G. A., et al. 1981, *ROAn*, **14**, 73
- Wright, C. O., Egan, M. P., Kraemer, K. E., & Price, S. D. 2003, *AJ*, **125**, 359
- Wright, E. L., Eisenhardt, P. R. M., Mainzer, A. K., et al. 2010, *AJ*, **140**, 1868
- Xing, L. F. 2010, *ApJ*, **723**, 1542
- Zuckerman, B. 2019, *ApJ*, **870**, 27
- Zuckerman, B., & Song, I. 2004, *ARA&A*, **42**, 685
- Zuckerman, B., Song, I., & Bessell, M. S. 2004, *ApJL*, **613**, L65
- Zuckerman, B., Song, I., Bessell, M. S., & Webb, R. A. 2001a, *ApJL*, **562**, L87
- Zuckerman, B., Song, I., & Webb, R. A. 2001b, *ApJ*, **559**, 388